

PNNL-35939-1

Real-Time Xenon Sensor Analysis Report

April 2025

SC Stave

KL Bertschinger

SB Emmons

EM Becker

JD Fast

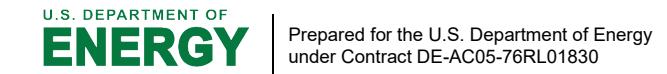
ER Siciliano

MJ Myjak

MA Zalavadia

AA Gowardhan*

*Lawrence Livermore National Laboratory



DISCLAIMER

This report was prepared as an account of work sponsored by an agency of the United States Government. Neither the United States Government nor any agency thereof, nor Battelle Memorial Institute, nor any of their employees, makes any warranty, express or implied, or assumes any legal liability or responsibility for the accuracy, completeness, or usefulness of any information, apparatus, product, or process disclosed, or represents that its use would not infringe privately owned rights. Reference herein to any specific commercial product, process, or service by trade name, trademark, manufacturer, or otherwise does not necessarily constitute or imply its endorsement, recommendation, or favoring by the United States Government or any agency thereof, or Battelle Memorial Institute. The views and opinions of authors expressed herein do not necessarily state or reflect those of the United States Government or any agency thereof.

PACIFIC NORTHWEST NATIONAL LABORATORY

operated by

BATTELLE

for the

UNITED STATES DEPARTMENT OF ENERGY

under Contract DE-AC05-76RL01830

Printed in the United States of America

Available to DOE and DOE contractors from the Office of Scientific and Technical Information, P.O. Box 62, Oak Ridge, TN 37831-0062

ph: (865) 576-8401 fox: (865) 576-5728 email: reports@osti.gov

Available to the public from the National Technical Information Service 5301 Shawnee Rd., Alexandria, VA 22312 ph: (800) 553-NTIS (6847) or (703) 605-6000

email: info@ntis.gov
Online ordering: http://www.ntis.gov

OBReal-Time Xenon Sensor Analysis Report

April 2025

SC Stave
KL Bertschinger
SB Emmons
EM Becker
JD Fast
ER Siciliano
MJ Myjak
MA Zalavadia

AA Gowardhan*
*Lawrence Livermore National Laboratory

Prepared for the U.S. Department of Energy under Contract DE-AC05-76RL01830

Pacific Northwest National Laboratory Richland, Washington 99354

Abstract

Abstract

Radiotracer release experiments were performed at the Nevada National Security Site in October 2022. The overall experiment was called the RElease ACTivity (REACT) experiment. Twenty-two real-time xenon sensors were deployed for each of four releases. Initial, quick-look analysis results were reported in December 2022. This report reviews the more comprehensive offline analysis effort that was conducted during the remainder of fiscal year 2023 by the Dynamic Networks venture. Improved energy stabilization routines were implemented along with an improved background subtraction routine compared to the original quick look calculations. The relative detection efficiencies of all real-time sensors were examined. Finally, simulated detector response functions were coupled to two different meteorological models using the measured conditions for the final release (REACT-04) to compare simulated detections with measurements. While there is some agreement between the models and measured data on the detection locations and timing, there is less agreement on the magnitude of those detections. Future sensor and meteorological modeling work will be needed to improve the agreement and to examine the additional releases (REACT-01 through REACT-03).

Abstract

Acknowledgments

This Low Yield Nuclear Monitoring (LYNM) research was funded by the National Nuclear Security Administration, Office of Defense Nuclear Nonproliferation Research and Development (NNSA DNN R&D). The authors acknowledge important interdisciplinary collaboration with scientists and engineers from Los Alamos National Laboratory, Lawrence Livermore National Laboratory, the Nevada National Security Site, Pacific Northwest National Laboratory, and Sandia National Laboratories.

Acknowledgments

Acronyms and Abbreviations

EWMA exponentially weighted moving average

FY fiscal year

MDA Minimum Detectable Activity

MET METeorological Nal sodium iodide

NNSS Nevada National Security Site

NSCRAD Nuisance-Rejection Spectral Comparison Ratio

PNNL Pacific Northwest National Laboratory

REACT RElease ACTivity experiment

REACT-N the Nth REACT release

ROI region of interest

Contents

Abstr	act			iii	
Ackn	owledgi	ments		iv	
Acror	nyms ar	nd Abbrev	iations	V	
1.0	Introd	duction		5	
2.0	Gain-	-Stabilizati	ion and Background Subtraction Procedure	8	
	2.1	Gain-St	tabilization Methods	8	
		2.1.1	Linear Fit Method	9	
		2.1.2	Linear Fit Results	9	
		2.1.3	Method of Moments	10	
		2.1.4	Method of Moments Results	11	
		2.1.5	Temperature Peak-Shift Correction Method	13	
		2.1.6	Temperature-Shift Method Results	13	
	2.2	Backgro	ound Subtraction Procedure	14	
		2.2.1	Spectra Summing	14	
		2.2.2	Summing Region of Interest	15	
		2.2.3	Exponentially Weighted Moving Average	15	
		2.2.4	EWMA Update Protocol	16	
		2.2.5	Background Subtraction	16	
		2.2.6	Statistical Uncertainty Propagation	17	
	2.3	Results	·	18	
		2.3.1	REACT-01	19	
		2.3.2	REACT-02	19	
		2.3.3	REACT-03	20	
		2.3.4	REACT-04	21	
	2.4	Synthet	tic Data Studies	22	
		2.4.1	Spectra Summing Effect on Timing	22	
		2.4.2	Synthetic Data Injected with Noise Performance	24	
	2.5	Spectra	l Anomaly Detection Method	27	
3.0	Nal D	etector R	elative Peak Efficiencies	29	
	3.1	Methodology			
	3.2	Efficiency Results Using Field Data			
	3.3	Efficiency Results Using Laboratory Data			
	3.4 Efficiency Analysis Summary				
4.0	Updated Detector Response Voxels			37	
5.0	Comparison of Experimental Data with Meteorological Modeling Results				
	5.1	5.1 FLEXPART-WRF			
	5.2	Aeolus		40	

	5.3	Discussion	41
6.0	Summ	ary and Future Work	43
7.0	Refere	ences	44
Appe	ndix A -	- EWMA Uncertainty Derivation	A.1
		- Detector Locations	
Figu	ıres		
Figure	e 1. Map	of sensor locations for REACT-04. Red dots are NaI sensors. White dots are meteorology stations. The shading is topography. The distance from sensor 1 to 18 is 4.7 km.	6
Figure	2. Unc	orrected spectrum for Nal-01 during REACT-01. The gain shift near channel 1000 over the course of the day is about 50 channels (5%)	9
Figure	: 3: Pea	k 1 is the continuum with a peak at about 80 keV, and Peak 2 is the K-40 peak at about 1,460 keV. Summing spectra improves the gain stabilization of the linear fit between peaks, but shows diminishing returns as the number of summed spectra inceases	10
Figure	4: Plot	s of moment corrected centroid location as a function of time for a transported detector (top) and a stationary detector (bottom). Figures on the left are for the first peak at 80 keV, and figures on the right are for the second peak at 1,460 keV. Top plots are for REACT-01 Nal-00, and bottom plots are for REACT-01 Nal-04. A.) The corrected centroid values for peak 1 at 80 keV and is from REACT -01. B.) The corrected values centroid for peak 2 at 1,460 keV and is from REACT-01. C.) The corrected centroid values for peak 1 at 80 keV and is from React -04. D.) Corrected centroid values for peak 2 at 1,460 keV.	
Figure	e 5: Gair	n-stabilization mean and standard deviation for each detector in each REACT release after applying the temperature peak-shift correction method. The top left is REACT-01, the top right is REACT-02, the bottom left is REACT-03, and the bottom right is REACT-04. REACT-01 and 02 had the same detector locations with releases happening at different times during the test day.	14
Figure	e 6: EWI	MA applied to two detections from REACT-04. The figure on the left shows EWMA applied to a time series with a substantial detection of radioxenon, and the figure on the right shows a marginal detection of radioxenon. In both cases, the EWMA can follow the random fluctuations naturally present in the time series. The time axis shows the hours, minutes, and seconds relative to the REACT-04 release time	
Figure	97: Exa	mple of the update protocol implemented with the EWMA for two cases where radioxenon is detected in the signal. In both cases, the EWMA becomes nearly constant in value once the count rate increases. The time axis shows the hours, minutes, and seconds relative to the REACT-04 release time.	16
Figure	8: Exa	mple of Xe-127 ROI count rate with propagated error bars	17

REACT-01. Count rates are for the Xe-127 ROI region from 20 to 220 keV. Only NaI-01 and NaI-02 show detections	19
Figure 10: Background subtraction procedure described in Section 2.2 applied to REACT-02. Count rates are for the Xe-127 ROI region from 20 to 220 keV. Only NaI-00 and NaI-03 show detections	20
Figure 11: The background subtraction procedure described in Section 2.2 applied to REACT-03. Count rates are for the Xe-127 ROI region from 20 to 220 keV. Only NaI-01made a detection at the 5 sigma level	21
Figure 12: The background subtraction procedure described in Section 2.2 applied to REACT-04. Count rates are for the Xe-127 ROI region from 20 to 220 keV. NaI-00, NaI-01, NaI-03, NaI-08, NaI-13, and NaI-21 made detections.	22
Figure 13: Artificial detection created to demonstrate the effect of summing spectra. Summing spectra shifts the start of the count increase for a detection, causes the detection width to widen, and the height to decrease.	24
Figure 14: Synthetic detection signal consisting of different widths created from a background spectrum and a spectrum with a radioxenon detection	25
Figure 15: Synthetic signal with a low amount of noise injected. The detections are easy to see, and summing the spectra smooths the detections.	26
Figure 16: Synthetic signal with a high amount of noise injected. The detections are difficult to see when analyzing the initial signal. Summing the spectra smooths the detection, making the detection more apparent. In addition, summing a random signal creates a random fluctuation	27
Figure 17: Two real-time xenon sensors undergoing energy calibration and efficiency testing at the NNSS. A Cs-137 source is on the tripod between the two sensors.	29
Figure 18: Cs-137 spectrum collected with the Nal-00 detector showing counts versus channels. The photopeak fit function and background curves are shown in the solid crimson line and dot-dashed black lines, respectively.	30
Figure 19: Relative peak efficiency plotted versus detector label. The solid dots correspond to the efficiency values and the error	32
Figure 20: A comparison of typical spectra from detectors Nal-15 and Nal-17 shows that the latter consistently has a slightly larger peak area (2673 counts vs. 2198 counts), while both have a larger peak area than Nal-00 (1632 counts) shown in Figure 18. Greater areas correspond to greater peak efficiencies for equal live times for measurements of the same source activity, assuming the source to detector distance was the same	33
Figure 21: The left figure is an unshielded spectrum taken with the Nal-01 detector. The 32 keV X-ray is more prominent in the unshielded spectrum than in that shown at right taken with Nal-02 in a shielded configuration with the source just outside of the shielding. The vertical axis is logarithmically scaled in each spectrum.	34
Figure 22: Peak count rate shown by the detectors. Note that only detectors Nal-01 through Nal-20 were tested in this fashion. The peak count rates vary about the expected value of 290 cps. Also note the suppressed zero on the v axis.	35

Figure 23: The relative peak efficiencies are obtained by dividing each peak count rate and uncertainty by the expected value of 290 cps. The resulting relative measures of efficiency show a greater consistency than the efficiencies plotted in Figure 19. Note the suppressed zero on the y axis	35
Figure 24. Top-view diagram of the symmetric quadrants around the central detector (star) that were used for the 100 meter voxels (Q1, upper right quadrant). The Qs refer to the quadrant number	37
Figure 25: Comparison of original and new detector response voxels at X = 10 m. From left to right is steps in z of 20 m centered at 10, 30, 50, and 70 m. Top to bottom is steps in y of 20 m centered at 10, 30, 50, and 70 m	38
Figure 26: Comparison of REACT-04 counts versus time in the 20–220 keV ROI with FLEXPART-WRF calculations for 6.3 m/s, 6 degrees, and stable conditions	40
Figure 27: Comparison of REACT-04 counts versus time in the 20–220 keV ROI with Aeolus calculations for 4 m/s, 350 degrees, and neutral conditions	41
Tables	
Table 1: The mean and standard deviation for each detector throughout the series of measurements after applying the method of moments. REACT-01 Nal-00 was moved during testing, which caused a large shift using the method of moments that resulted in a high standard deviation	13
Table 2: Summary of detections for REACT-01	19
Table 3: Summary of detections for REACT-02	20
Table 4: Summary of detections for REACT-03	21
Table 5: Summary of detections for REACT-04	21
Table 6: Relative detector efficiency normalized to detector NaI-00 and the corresponding uncertainty.	32
Table 7: Sensor locations for REACT-01 and REACT-02	B.1
Table 8: Sensor locations for REACT-03	B.2
Table 9: Sensor locations for RFACT-04	B 3

1.0 Introduction

During the RElease ACTivity experiment (REACT), radioxenon gas (Xe-127) was released, and 2"×4"×16" (5×10×40 cm) thallium-doped sodium iodide (NaI(TI)) detectors (Stave, et al., In process) were deployed at the Nevada National Security Site (NNSS) to monitor the migration of the gas. The long axis of the detectors was vertical with the 4"×16" face facing north. The specific locations for one of the releases are shown in Figure 1 and can be found in Appendix B. The detectors were placed on arcs approximately 0.5, 2.0, 3.5 and 4.5 km from the release point with some detectors placed at close range. The configuration of the detectors was changed between some of the releases to increase the probability that detectors would have positive detections.

To correctly quantify possible detection, a background subtraction algorithm was designed and implemented. There were four, five-minute-long releases of Xe-127 gas that took place with the releases labeled REACT-01, REACT-02, REACT-03, and REACT-04. The first two releases occurred during one day and the following two each happened on a different day. Twenty-two different NaI detectors (designated NaI-XX for XX from 00 to 21) were deployed in multiple configurations over the course of the four releases. The original deployment design was used for REACT-01 and REACT-02 but then NaI-00 was moved closer to the release point for REACT-03. NaI-01, NaI-08, NaI-13, and NaI-15 were then all moved to closer positions for REACT-04 to better instrument the close-in region.

Gamma-ray spectra were captured by each Nal detector at 20-second intervals throughout the day, resulting in 4,320 spectra to potentially analyze per detector. The first several hours of collected spectra provides a good characterization of the background. With the radiotracer releases scheduled near sunrise (for forecasted optimal weather conditions), there was a natural temperature change that caused a gain shift for all detectors, which was expected. The need for offline analysis to correct the gain had been anticipated. To process the data, spectra collected approximately 30 minutes before and 60 minutes after the release were selected. The spectra were first gain-stabilized to correct for this shift. To improve the statistics, the spectra were then summed over time in a running average to reduce the counting uncertainty and then normalized by live time to obtain a count rate. Next, the spectra channels were summed over a defined region of interest (ROI) from 20 to 220 keV (corresponding to the energies and down scatter region for the main gamma rays emitted by Xe-127) to create a time series of count rates. With the data converted to a series of ROI count rates over time, the background rate could be characterized using spectra from well before and after the release and then subtracted for each collected ROI with potential counts due to the release. To adapt for the changing background, an exponentially weighted moving average (EWMA) was implemented. To avoid subtracting possible radioxenon detections, a rule was added so that the EWMA would not update when the count rate increased by a certain set amount. The background subtraction method was applied to each Nal detector, and the detections of radioxenon were identified.

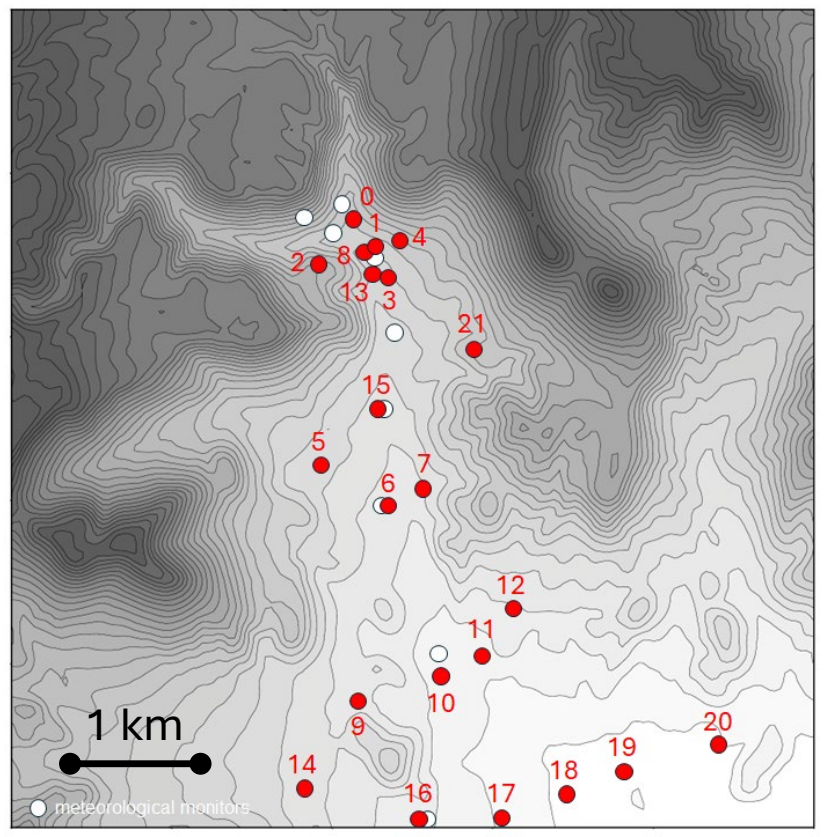


Figure 1. Map of sensor locations for REACT-04. Red dots are Nal sensors. White dots are meteorology stations. The darker shading indicates elevated topography. Topography data is from the United States Geological Survey 1-arcsecond Digital Elevation Model.

Laboratory and field measurements were performed on each of the 22 NaI sensors to ensure their performance in the field would be understood. The detection efficiency, initial energy calibration, and energy resolution were all determined in the laboratory at Pacific Northwest National Laboratory (PNNL) months prior to deployment using a calibrated gamma-ray source. To verify the detectors were all still performing as expected after shipment to the NNSS and just prior to deployment, another set of measurements was performed. The goal of those measurements was to verify that the energy resolution and calibration were still within defined experimental tolerances (better than 9% at 662 keV for the energy resolution; 0 to 3 MeV full range for the energy calibration). All systems were determined to be performing as expected. The results of both the laboratory and field measurements are presented.

The radioxenon detections observed during REACT-04 were compared with predictions from two meteorological (MET) models: Aeolus (Gowardhan, et al., 2021), a computational fluid dynamics model using a Large Eddy Simulation method designed for efficient and accurate simulations of local terrain and small feature effects, and FLEXPART-WRF (Brioude, et al., 2013), a Lagrangian particle dispersal model that uses local terrain. These MET model predictions used a 1-arcsecond (~30 m) digital elevation model from the United States Geological Survey and were combined with a simulated detector response function based on a voxel approach. The volume surrounding each detector was broken up into smaller regions of Xe-127 source gas. The amount of gas in each voxel was determined by the MET models. These large volume simulations were combined with the time dependent predictions from the MET models to generate simulated counts that were then processed in the same way as the

measured data (time averaged and smoothed) and then compared with the measured data. Additional iterations with the MET modeling teams are expected to improve the agreement. However, the initial comparisons were quite favorable as to the sensors with positive and negative detections, the timing, and the approximate magnitude of the detections.

2.0 Gain-Stabilization and Background Subtraction Procedure

One goal of the measurement campaign is to have statistically defendable detections of the radiotracer that are known in time and location. Positive detections are relatively simple when there are many counts. The spectrum can be examined for the tell-tale energies associated with the Xe-127 radiotracer and there are significant elevations in the count rate. However, near the limits of detection, statistical tests need to be applied. As will be detailed below, a 5σ cut-off value was chosen to discriminate between random fluctuations and likely detections. However, before that statistical test can be applied, the spectra needed to be gain-stabilized and background subtracted. Once that has been accomplished, the statistical variation in the background can be used to determine the 5σ threshold. Details about the gain-stabilization methods, background subtraction procedures and results are presented.

2.1 Gain-Stabilization Methods

Throughout the course of the day, the temperature varied by tens of degrees Fahrenheit and caused the gain for the detectors to shift (typically about 2% during a radiotracer release). An example of the gain shift is shown in Figure 2. To sum spectra and determine counts in an ROI, the gain must be stabilized throughout the course of the measurements. To gain-stabilize the data, three algorithms were implemented and tested. First, a fit and linear calibration was performed on the gamma spectrum looking at the continuum peak and K-40 peak at 1,460 keV. The second method utilizes moments to correct for the gain shift (Mitra, 2016). The last method calculates the shift between spectra at a gamma peak, and uses that information to calculate the shift correction (Casanovas, Morant, & Salvado, 2012). The last method was the one selected to be applied to the data because it resulted in the most stable spectra over time.

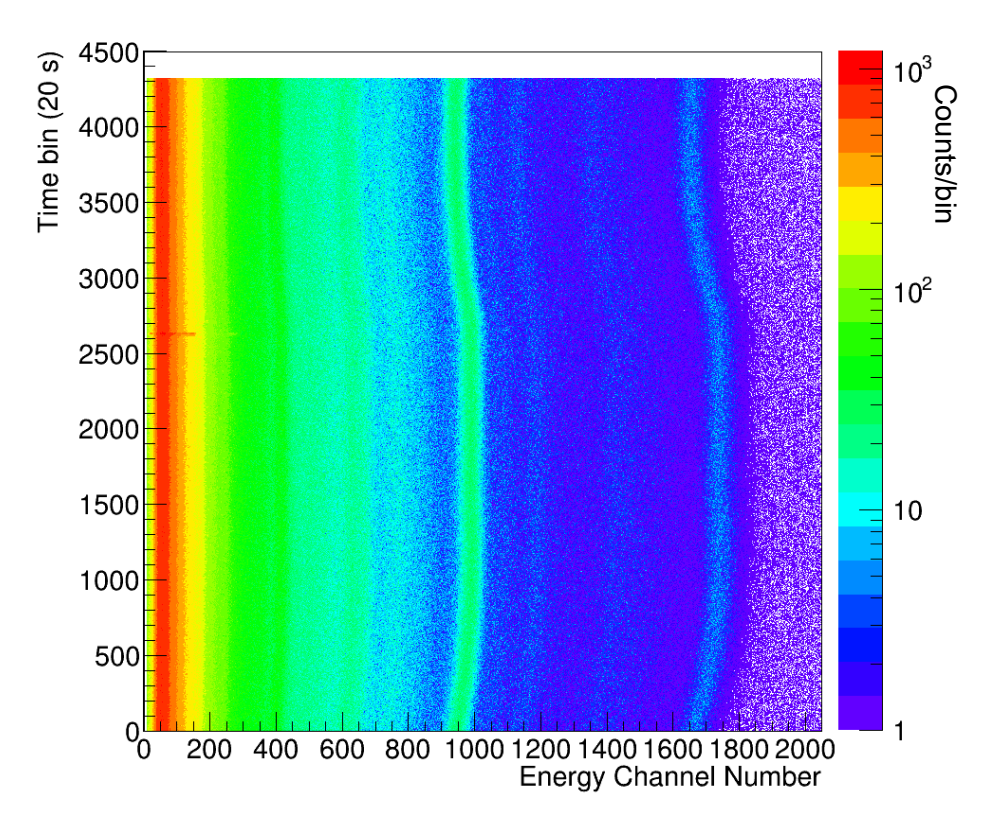


Figure 2. Uncorrected spectrum for NaI-01 during REACT-01. The gain shift near channel 1000 over the course of the day is about 50 channels (5%).

To quantify the correctness of the gain-stabilizing procedure, a Gaussian function was independently fit to two peaks occurring throughout the spectrum after a gain-stabilization method is applied. The first peak is the continuum peak produced in the gamma spectrum at about 80 keV, and the second peak is the naturally occurring K-40 line at 1,460 keV. Though the continuum peak is not a true peak, a Gaussian function can be fitted similarly to the K-40 peak and the feature appears in the same location for all the real-time xenon sensors.

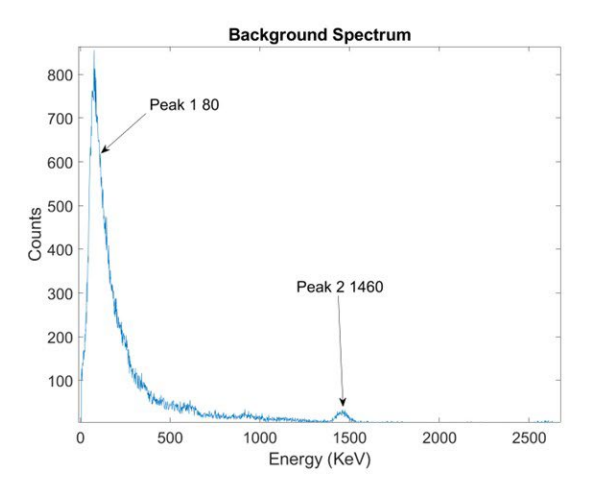
2.1.1 Linear Fit Method

The first gain-stabilization method applied a linear fit between two peaks present in the dataset to obtain a new calibration for each spectrum. The first peak was the continuum peak formed around 80 keV. The second peak is the 1,460 keV peak from K-40. To improve the fitting and obtain a better linear fit between points, spectra were summed iteratively over 20 to 100 seconds. After summing the spectra, the peak position was found by fitting a Gaussian function and fitting a line between the two points. This results in a gain value and offset that can be applied to correct the spectrum.

2.1.2 Linear Fit Results

The average and standard deviation were found for the 80 and 1,460 keV fitted peaks. As seen in Figure 3, the standard deviation improves when the spectra were summed. Overall, the standard deviation for peak 1 is approximately 2.5 keV, and the standard deviation of peak 2 is less than 1 keV. Summing spectra decreases the standard deviation, but only slight improvements were observed. The method worked well, but in a few rare cases in the dataset, it

failed to find a linear fit. In addition, a higher performing method was identified (see Section 2.1.6). Overall, as shown in Figure 3, the 100 second summing performed the best. There appeared to be diminishing returns if the summing time was extended.



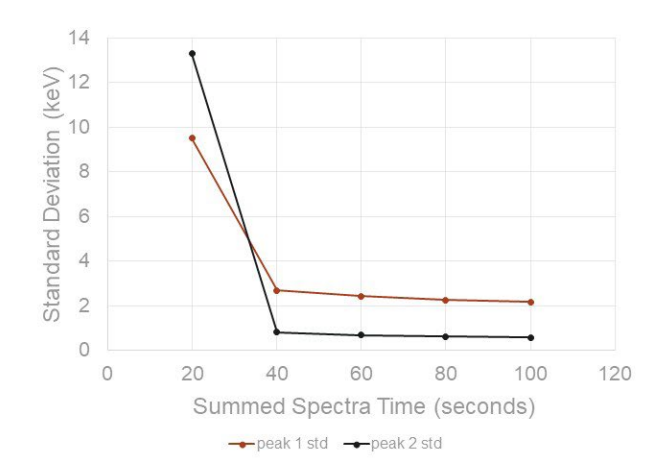


Figure 3: Peak 1 is the continuum with a peak at about 80 keV, and Peak 2 is the K-40 peak at about 1,460 keV. Summing spectra improves the gain stabilization of the linear fit between peaks, but shows diminishing returns as the number of summed spectra inceases.

2.1.3 Method of Moments

The second method investigated was the method of moments from (Mitra, 2016). This method assumes that the spectra taken later with a different temperature are the same except for some transformation that has occurred $X(\xi)$. Therefore, the moments for each spectrum are the same, and the transformation $X(\xi)$ can be found by taking the moment of each spectrum and solving for $X(\xi)$. The full derivation can be found in (Mitra, 2016), and only a brief synopsis of the method is provided in this report. First, the transformation is assumed to be first order with $X(\xi) = a_0 + a_1 i$, where i is the channel. The coefficients are given as

$$a_0 = \frac{\mu_1}{\mu_0} - a_1 \frac{m_1}{m_0}$$

and

$$a_1 = + \sqrt{\frac{\frac{\mu_2}{\mu_0} - \frac{\mu_1^2}{\mu_0^2}}{\frac{m_2}{m_0} - \frac{m_1^2}{m_0^2}}}$$

The value m_k is the k-order moment for the initial spectrum, and μ_k is the k-order moment for the next spectrum. The initial spectrum is assumed to be corrected while the next spectrum needs to be corrected to match the initial spectrum. Solving for the moments in each subsequent spectrum and transforming the spectrum to match the initial spectrum results in a gain-stabilized dataset.

2.1.4 Method of Moments Results

This method works well for correcting the gain shift. However, as shown in the top plots of Figure 4, when the NaI-00 detector was moved to a different location (between REACT-02 and REACT-03), the gain-stabilized spectra peaks shifted substantially to the wrong location. However, this is an artifact of the analysis. The method assumes no true change in the underlying spectrum which is likely violated when the detector is moved to a new location. In the case when the detector was not moved (Figure 4, bottom), the algorithm worked as intended with about 2% deviation from the mean for peak 1, and less than 1% standard deviation for peak 2. The main advantage of the method of moments is the ability to gain-stabilize spectra quickly. An entire REACT release consisting of 22 detectors with approximately 4,000 measured spectra can be gain-stabilized in less than 1 minute on a standard laptop computer (intel i7 CPU). Subsequently, the accuracy of the method is comparable to the linear fit method discussed in Section 2.1.1. As will be shown in Section 2.1.6, another method was found with even better performance. The gain-stabilization results are summarized in Table 1.

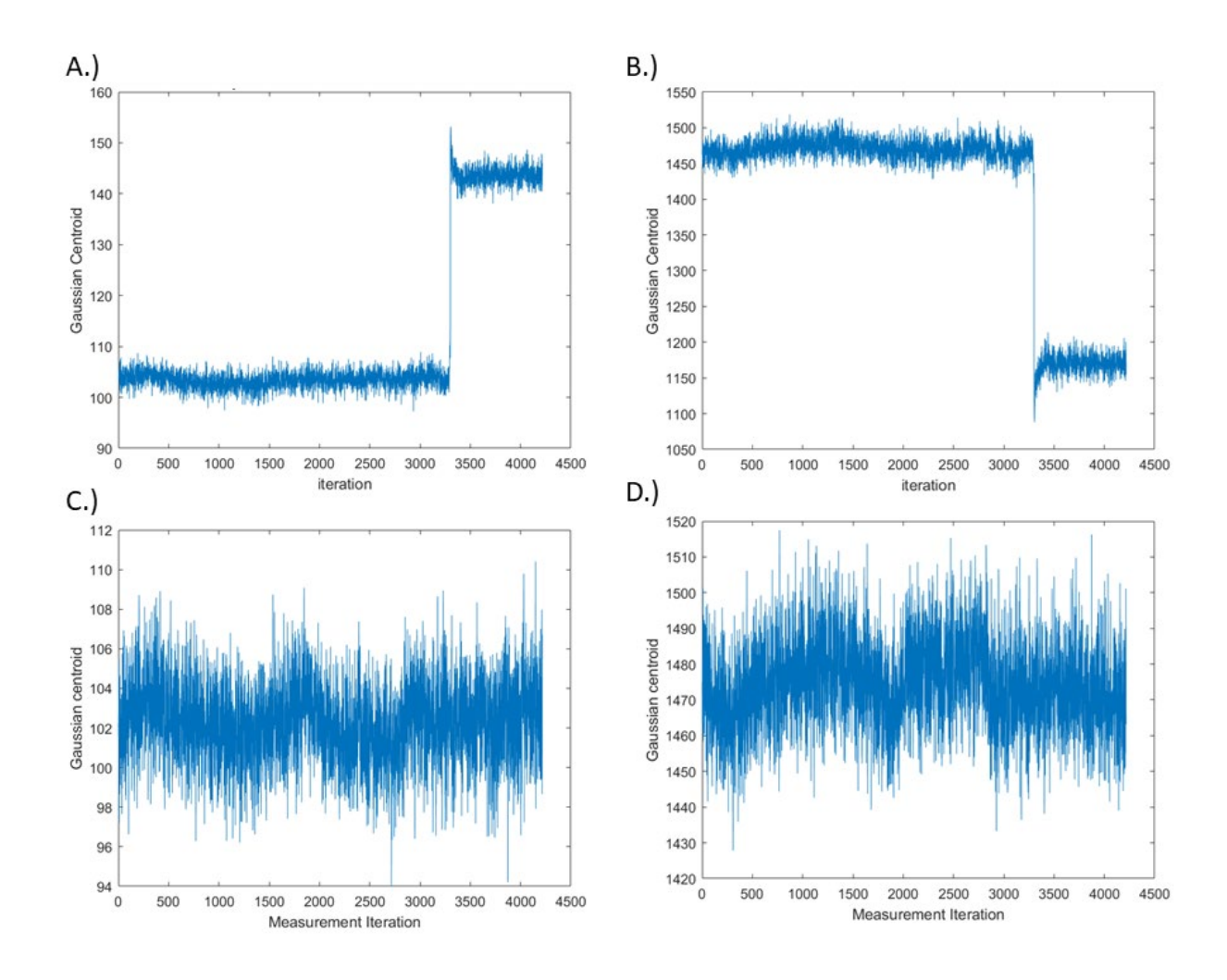


Figure 4: Plots of moment corrected centroid location as a function of time for a transported detector (top) and a stationary detector (bottom). Figures on the left are for the first peak at 80 keV, and figures on the right are for the second peak at 1,460 keV. Top plots are for REACT-01 Nal-00, and bottom plots are for REACT-01 Nal-04. A.) The corrected centroid values for peak 1 at 80 keV and is from REACT-01. B.) The corrected values centroid for peak 2 at 1,460 keV and is from REACT-01. C.) The corrected centroid values for peak 1 at 80 keV and is from React -04. D.) Corrected centroid values for peak 2 at 1,460 keV.

Table 1: The mean and standard deviation for each detector throughout the series of measurements after applying the method of moments. REACT-01 Nal-00 was moved during testing, which caused a large shift using the method of moments that resulted in a high standard deviation.

	Centroid position	Mean	Standard deviation	Percent
REACT-01 Nal-00	Peak 1	112	16.69	14.9%
REACT-01 Nal-00	Peak 2	1404	125.089	8.9%
REACT-01 Nal-04	Peak 1	102.29	2.08	2.03%
REACT-01 Nal-04	Peak 2	1474.4	12.66	0.86%

2.1.5 Temperature Peak-Shift Correction Method

The peak-shift correction method was taken from (Casanovas, Morant, & Salvado, 2012). The method consists of finding the gain shift between two spectra and using that information to correctly shift one spectrum to match the other. First, let a channel be given by C_{ik} with i as the channel number and k as the spectrum in a series of measurements. A key observation from (Casanovas, Morant, & Salvado, 2012) is that the change in temperature only affects the gain of a NaI or lanthanum bromide detector, so an offset does not need to be found between subsequent spectra. This implies that under constant voltage, the digitizer channel position corresponding to the deposited energy only depends on temperature, so a relationship between the i^{th} channel C_{ik} and initial channel C_{i0} can be given by

$$C_{ik} = C_{i0} f(T_k)$$

with $f(T_k)$ as a transfer function between the channels in the two different spectra. It is assumed that the shift is the same for all channels for each spectrum such that $f_1(T_k) \approx f_2(T_k) \approx \cdots f_n(T_k) = f(T_k)$.

By finding the function $f(T_k)$, shifts in the spectra, caused by temperature change, can be corrected. As shown in (Casanovas, Morant, & Salvado, 2012), the transfer function can be found with $f(T_k) = \frac{c_{i0}^{known}}{c_{ik}^{known}}$. Using the 1,460 keV peaks as the known line and fitting a Gaussian function to each of the K-40 peaks in each subsequent spectrum, the current peak position in the uncorrected spectrum was found. The transfer function $f(T_k)$ can be found and then applied to each channel to gain-stabilize the spectrum.

2.1.6 Temperature-Shift Method Results

The effectiveness of the correction method was characterized by fitting a Gaussian peak to the two observed peaks in the spectrum like the other gain-stabilization methods. Then, the centroid values are averaged, and the standard deviation is found for each detector in a release. Overall, the standard deviation is less than 0.1% for both the 80 keV and 1,460 keV continuum peaks for each detector in each release. Because the temperature-shift method provided the most consistency, the method was used to gain-stabilize the dataset. An example of the consistency is shown in Figure 5.

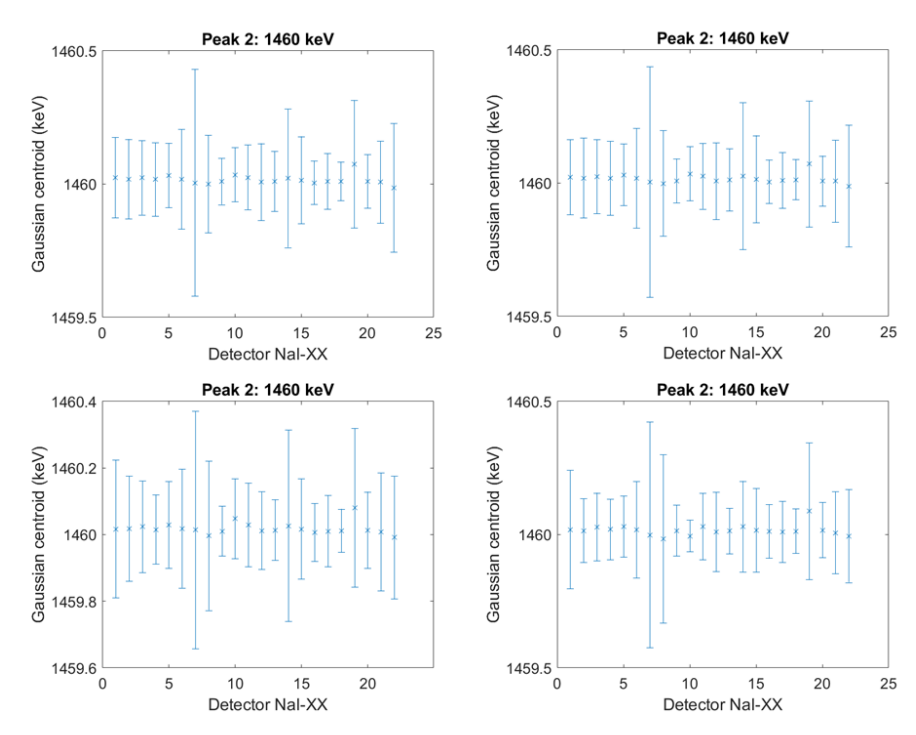


Figure 5: Gain-stabilization mean and standard deviation for each detector in each REACT release after applying the temperature peak-shift correction method. The top left is REACT-01, the top right is REACT-02, the bottom left is REACT-03, and the bottom right is REACT-04. REACT-01 and 02 had the same detector locations with releases happening at different times during the test day.

2.2 Background Subtraction Procedure

Once each spectrum has been gain-stabilized and the array of spectra has been restructured, the spectra can be summed for an arbitrary number of time steps. The gamma spectra are recorded at 20 second intervals, and it is unknown when exactly a detection will occur. For this reason, spectra are summed continuously moving forward in time for the desired number of iterations. The spectra are then summed over an ROI to create a time series. Then, an exponentially weights moving average (EWMA) is applied to the time series to characterize the background. The EWMA is then subtracted from the signal. An increase in the count rate over this background indicates where the radioxenon detections have occurred. Lastly, an update protocol is introduced to avoid including detections in the background estimate, and the statistical uncertainty is propagated.

2.2.1 Spectra Summing

The summing procedure applies a rolling window forward in time. The first step is to sum the spectrum and live time forward in time for a given number of iterations. For example, when summing 5 spectra, start at spectrum 1 and sum to spectrum 5—the summed spectra will now be at the spectrum 1 position in time. Then, starting at spectrum 2, sum up to spectrum 6—this spectra sum will now be at the spectrum 2 position in time. Because the spectra are being summed forward in time, this causes detection events to appear earlier in time by the number of spectra summed. To account for this, the summed spectra are placed forward in time by the number of spectra summed. The effect of timing is discussed in more detail in Section 2.4.1.

The next step is to convert the summed spectrum to counts per second by dividing it by the summed live time.

2.2.2 Summing Region of Interest

After the data have been summed for a given number of spectra and converted to a count rate, the data can now be observed for finding a detection. Detection can be determined by observing an increase in the net count rate across a series of measurements in time. It is impractical to look at the spectra for each measurement, so summing over a predefined ROI can convert the series of spectra measurements to a time series of data points with different count rates. The spectra were summed for an ROI of 20 keV to 220 keV, corresponding to the energies and downscatter region for Xe-127.

2.2.3 Exponentially Weighted Moving Average

EWMA is a smoothing technique that uses an exponentially weighted window over a time series. EWMA was selected over other more simple methods due to the expectation that it would be less susceptible to gain shifts and changes in background over time. The EWMA (Box, Luceno, & del Carmen Paniagua-Quinones, 2011) is defined recursively as

$$v_i = (1 - \alpha)v_{i-1} + \alpha r_i$$

where v_i is the EWMA, α is the smoothing parameter, v_{i-1} is the previous EWMA value in the time series, and r_i is the signal or initial time-series data. As the function is applied over the signal, the weighting term decays exponentially going back in time from the current time step. The weight term can be expressed as $w_n = \alpha(1-\alpha)^n$. Subsequently, the number of terms included in the weighted sum can be found with $\alpha = \frac{2}{n+1}$. An example of the EWMA for smoothing over the time series for 45 iterations or 900 seconds is shown in Figure 6.

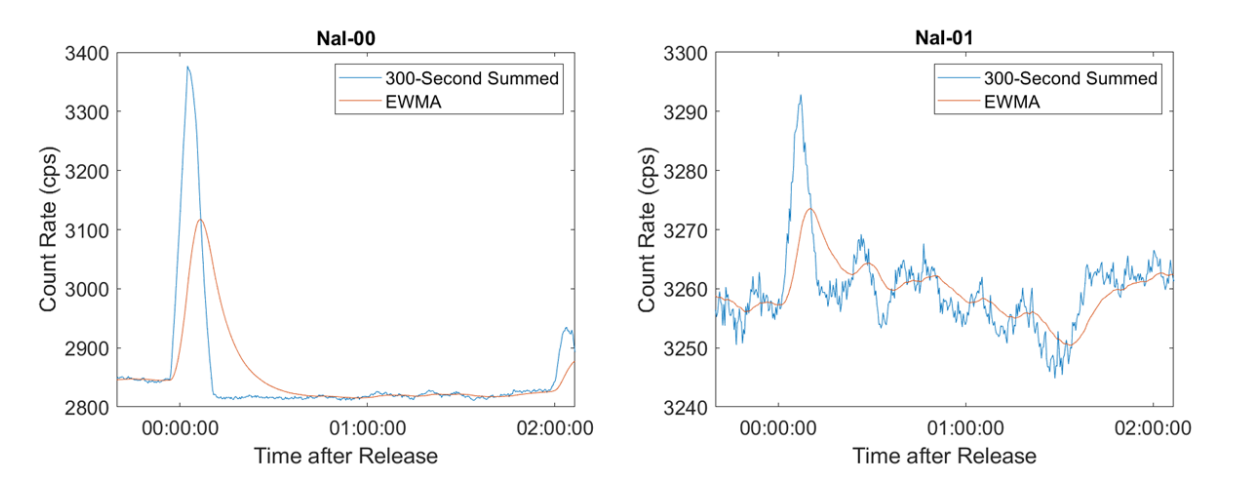


Figure 6: EWMA applied to two detections from REACT-04. The figure on the left shows EWMA applied to a time series with a substantial detection of radioxenon at the start of the radiotracer release with a second detection two hours later (during the purge of the release system). The figure on the right shows a marginal detection of radioxenon peaking about ten minutes after the release. In both cases, the EWMA can follow the random fluctuations naturally present in the time series. The time axis shows the hours, minutes, and seconds relative to the REACT-04 release time.

2.2.4 EWMA Update Protocol

When applying an EWMA, the background should be subtracted, but not the counts from the true source. To avoid over-subtracting counts from the source, an update protocol was implemented. The EWMA algorithm is set to not update the background estimate when the count rate increases by a user-defined threshold. That is updated every 20 seconds as a new summed spectrum region becomes available. This keeps the background flat over a detection event, and none of the counts from the detection event are removed. Ideally, a detection will occur when the signal exceeds the standard deviation above the background. This can be found by subtracting the EWMA from the measured signal. To be conservative and not include radiotracer in the background, a 1 standard deviation threshold was chosen and consistently applied to all the detectors. If the result is greater than 1 standard deviation, then that is considered the start of a detection of radioxenon in the signal and the EWMA will not update. If the converse is true, then the EWMA will be updated as normal. An example of the updated protocol applied to data is shown in Figure 7. The EWMA is clearly tracking the variations in background count rate but not including apparent increases due to the presence of radiotracer.

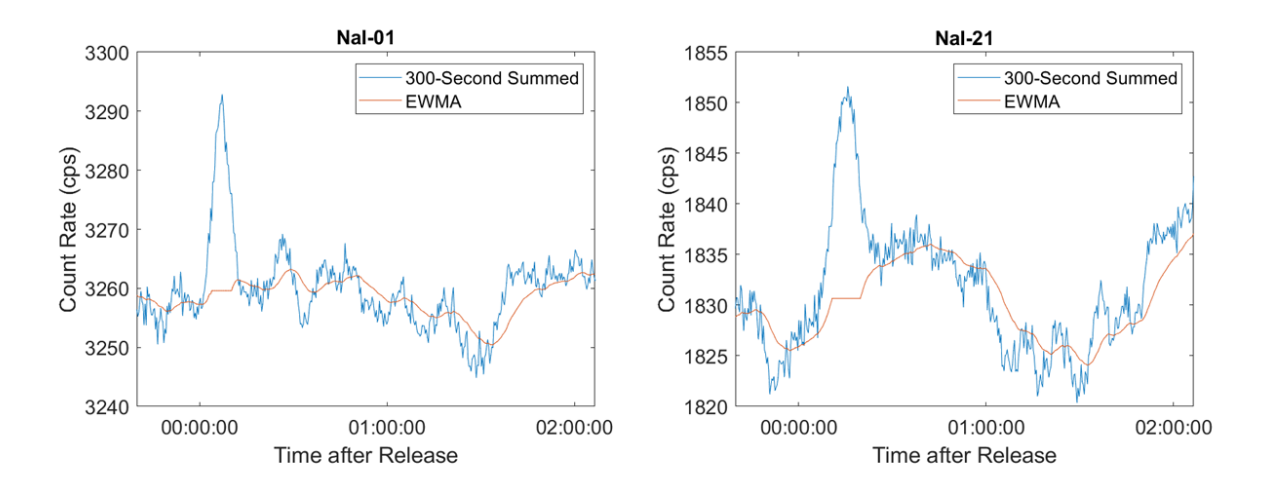


Figure 7: Example of the update protocol implemented with the EWMA for two cases where radioxenon is detected in the signal. In both cases, the EWMA becomes nearly constant in value once the count rate increases. The time axis shows the hours, minutes, and seconds relative to the REACT-04 release time.

2.2.5 Background Subtraction

The background subtraction is implemented by subtracting the EWMA from the summed signal. The EWMA is calculated from the initial signal, with each count rate coming from a 20-second measured spectrum. The EWMA is then smoothed over with an α parameter that corresponds to 45 measured spectra given by $\alpha = \frac{2}{n+1}$. This corresponds to a 900-second EWMA that gives a well-characterized background. Other EWMA smoothing times were not examined in this analysis. The 900 second time was chosen as a compromise between the 300 second integration time (driven by the 300 second radiotracer release time) for the analysis and the desire for small statistical uncertainty on the background. With the background changing over time, a significantly longer background (with its reduced statistical uncertainty) would add increased systematic uncertainty to the analysis. The EWMA smoothing time could also be potentially optimized in future work.

2.2.6 Statistical Uncertainty Propagation

For Poisson distributed counts above approximately ten counts, the statistical uncertainty in the counts is Gaussian and is given by $\sigma_c = \sqrt{c}$ with c being the total counts. The uncertainty in the count rate can be found with $\sigma_r = \frac{\sqrt{c}}{t}$ with t as the time of the measurement. The total counts c can be expressed as c = rt with r as the count rate. The count rate of the uncertainty is then $\sigma_r = \frac{\sqrt{rt}}{t} = \sqrt{\frac{r}{t}}$. The longer the time for the recorded spectrum, the lower the uncertainty in the count rate. In conjunction, the background is found by calculating the EWMA for the time series, and the uncertainty in the EWMA is given by:

$$\sigma_v = \sqrt{\frac{1-\alpha}{1+\alpha}}\sigma_r$$

and a derivation can be found in Appendix A (Box, Luceno, & del Carmen Paniagua-Quinones, 2011). Because the background subtraction is simply $N_i = r_i - v_i$, where N_i is the net count rate for time period i, r_i is the count rate for time period i, and v_i is the EWMA background count rate at time period i, propagating the uncertainty between the two terms is accomplished by adding the terms in quadrature. This gives

$$\sigma_{N_i}^2 = \sigma_{r_i}^2 + \sigma_{v_i}^2$$

$$\sigma_{N_i}^2 = \frac{r_i}{t} + \frac{1 - \alpha}{1 + \alpha} \sigma_{r_i^2}$$

An example of the propagated uncertainty is given in Figure 8.

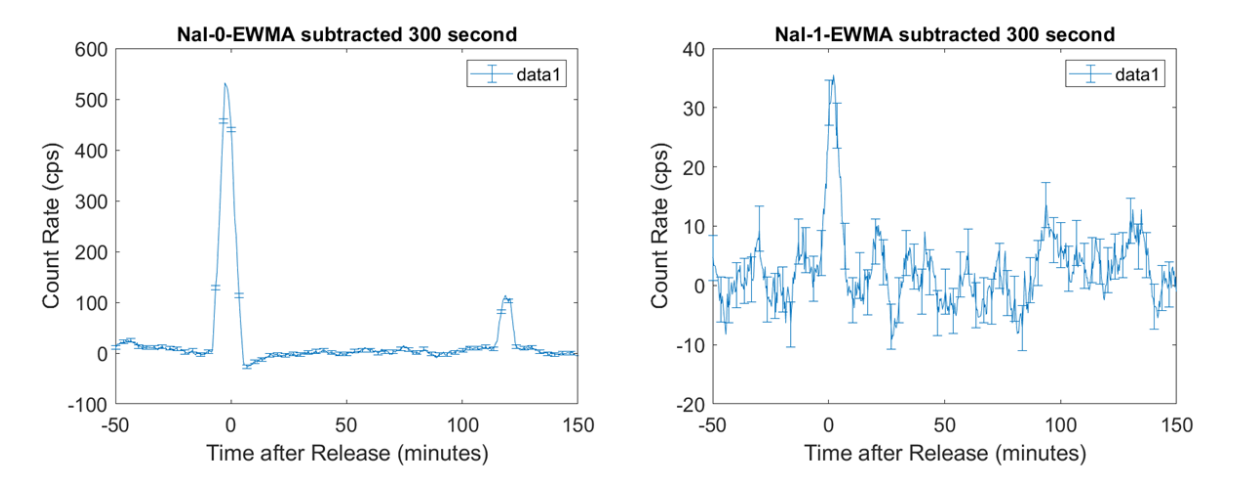


Figure 8: Example of Xe-127 ROI count rate with propagated error bars.

It should be noted that the variables σ_{r_i} and σ_{v_i} are not independent since the variable σ_{v_i} depends on the variable σ_{r_i} . The covariance of the two variables should be added to the uncertainty formula to obtain the correct uncertainty in the background subtracted counts. This results in the error propagation as

$$\sigma_{N_i}^2 = \sigma_{r_i}^2 + \sigma_{v_i}^2 + 2Cov(\sigma_r, \sigma_v)$$

 $\sigma_{N_i}^2 = \sigma_{r_i}^2 + \sigma_{v_i}^2 + 2 Cov(\sigma_r, \sigma_v)$ with $Cov(\sigma_r, \sigma_v)$ as the covariance between the variables σ_r and σ_v for an entire series of measurements. However, the covariance was calculated computationally for each series and found to be an order of magnitude lower than σ_r and σ_v . For this reason, the covariance term between σ_r and σ_v was ignored.

2.3 Results

The presence of radioxenon (Xe-127) gas was detected after applying the background subtraction procedure. The spectra were combined in a running sum of 15 measurements, corresponding to 300 seconds. Other summing times were investigated such as 60 seconds, 180 seconds, and 500 seconds. 300 seconds was chosen as the optimal time for this analysis and also corresponds to the release time. Longer integration times provide a better minimum detectable activity (MDA), however, times longer than 300 seconds can incorporate background counts which tends to minimizing the peak profile of a detection event. Shorter integration times provide better timing fidelity but decrease the MDA.

Next, the EWMA was smoothed with a α parameter corresponding to 45 measurements, which is equivalent to 900 seconds. The measured signal fluctuates randomly over time. The spectra summing in conjunction with this randomly fluctuation will cause the signal to increase and decrease in the form of a random fluctuations. This random walk creates peaks in the signal that can be mistaken for a detection. A way to increase confidence that a detection is real is to determine how many standard deviations above background the peak occurs. Empirically looking through the dataset there are clear detections and some cases that appear like detection due to random fluctuations. It was decided to apply a 5σ cut-off value to discriminate between random fluctuations and likely detections. Using an approximate version of the Currie equation (Currie, 1968) with acquisition time for the background equal to the measurement, if the signal is 4.65 standard deviation above the background then with 95% confidence the event is a detection. The Currie equation for a well-characterized background has a 3.29 standard deviation cutoff. This helps to give an idea of the expected range of sigma values to have 95% confidence in a detection. Those results are also based on pure statistics and there are systematic effects present due to the fluctuation in the background. A 5σ threshold was chosen so there is confidence that count rates above that threshold are true detections and not noise. With further modeling, anomalies and events with less than 5σ may be discerned as detections. However, for this report only detection events that are above 5σ will be considered detections.

To review, spectra were collected every 20 seconds. To better detect the present of radioxenon. spectra were combined in a running 5 minute sum to obtain a longer count time. This resulted in 5 minutes summed spectra being updated every 20 seconds. The time between these 20 second updates was interpolated to estimate time to the second.

Each detection is summarized in the table below for the respective REACT-N release. The time of detection corresponds to the time after the start of the radioxenon release and is given for the peak position of the detection. The standard deviation (sigma) was found as described in Section 2.2.6.

This analysis found that REACT-01 and -02 each had two detections. REACT-03 had one detection. Lastly, REACT-04 had the most detections with six. The details are described in the following subsections.

2.3.1 REACT-01

For REACT-01, only two detections were observed for detectors NaI-01 and NaI-02. The detections are displayed in Table 2, and the plots are displayed in Figure 9.

 REACT-01

 Detector
 Time of Peak (min:sec)
 Count Rate (CPS)
 sigma

 Nal-01
 5:43
 949
 177.43

 Nal-02
 7:15
 99
 20.08

Table 2: Summary of detections for REACT-01.

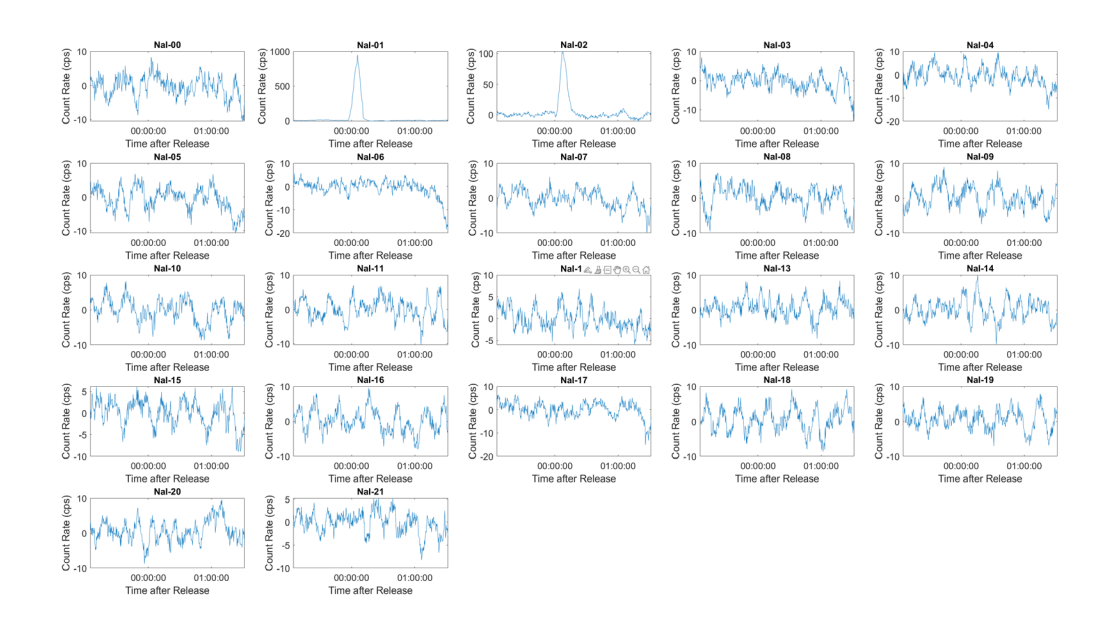


Figure 9: The background subtraction procedure described in Section 2.2 applied to REACT-01. Count rates are for the Xe-127 ROI region from 20 to 220 keV. Only NaI-01 and NaI-02 show detections.

2.3.2 REACT-02

Similar to REACT-01, REACT-02 had two observable detections. For REACT-02, the NaI-00 and NaI-03 detectors encountered radioxenon detections. The detections are displayed in Table 3, and plots are displayed in Figure 10.

Table 3: Summary of detections for REACT-02.

REACT-02				
Detector	Time of Peak (min:sec)	Count Rate (CPS)	sigma	
Nal-00	4:50	21	5.24	
Nal-03	8:57	35	6.78	

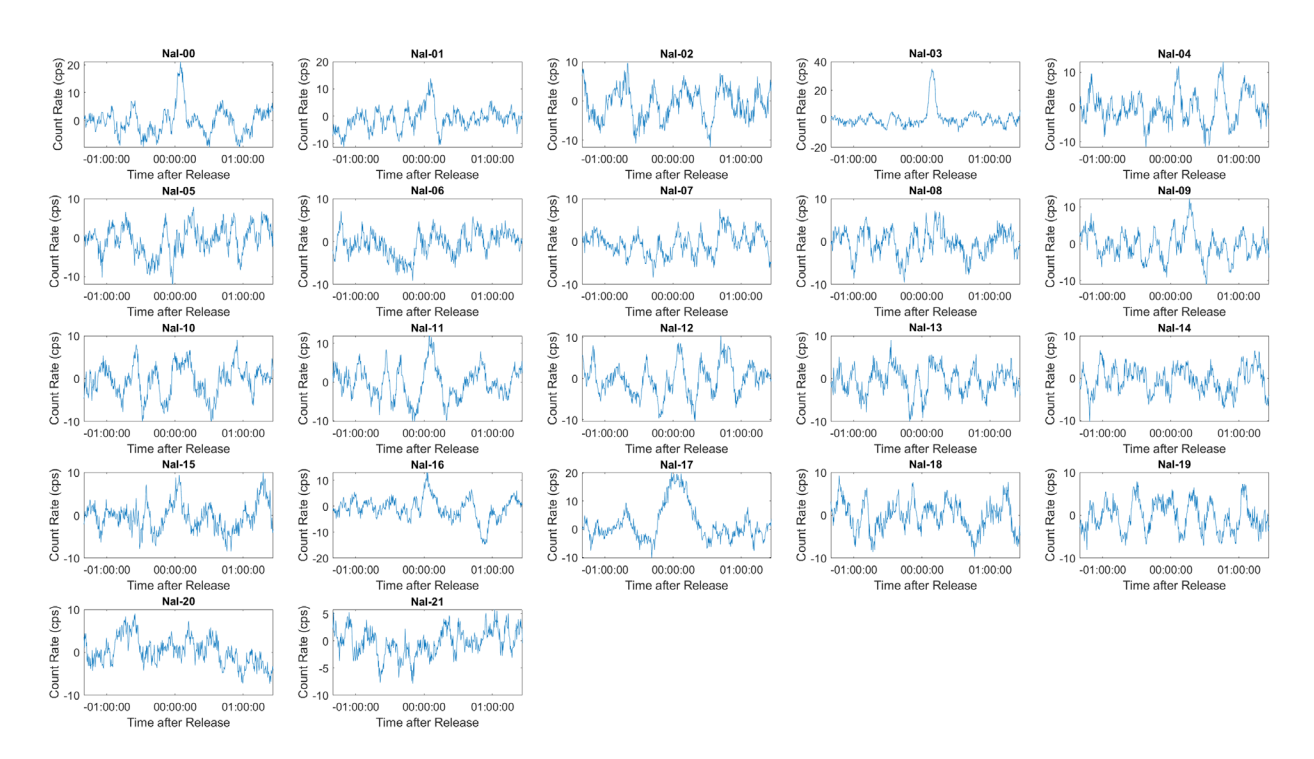


Figure 10: Background subtraction procedure described in Section 2.2 applied to REACT-02.

Count rates are for the Xe-127 ROI region from 20 to 220 keV. Only NaI-00 and NaI-03 show detections.

2.3.3 REACT-03

For REACT-03, one detection was observed at 5 sigma with three others having possible detections. Detector Nal-01had the one positive detection of radioxenon. The detection and possible detections are displayed in Table 4, and plots are displayed in Figure 11.

Table 4: Summary of detections for REACT-03.

REACT-03					
Detector	Time of Peak (min:sec)	Count Rate (CPS)	sigma		
Nal-01	5:23	521	104.74		
Nal-02	8:14	19.5	4.03		
Nal-06	13:45	18	4.84		
Nal-07	12:33	13	3.48		

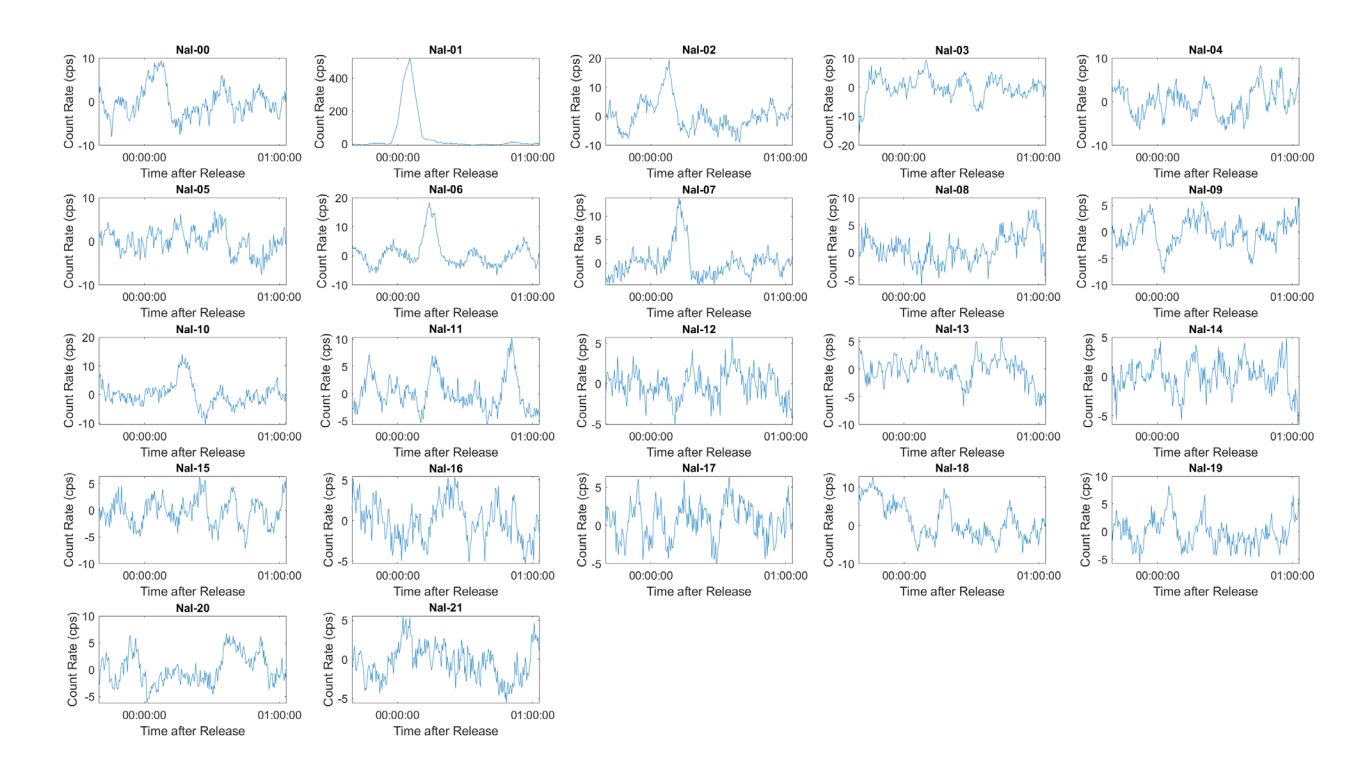


Figure 11: The background subtraction procedure described in Section 2.2 applied to REACT-03. Count rates are for the Xe-127 ROI region from 20 to 220 keV. Only NaI-01made a detection at the 5 sigma level.

2.3.4 REACT-04

REACT-04 saw the most detections with six. Nal-00, Nal-01, Nal-03, Nal-08, Nal-13, and Nal-21 detected radioxenon. The detections are summarized in Table 5, and the plots are displayed in Figure 12. Two near-detects on Nal-05 and Nal-07 were also included in the tables.

Table 5: Summary of detections for REACT-04.

REACT-04				
Detector	Time of Peak (min:sec)	Count Rate (CPS)	sigma	
Nal-00	2:26	551	118.8	
Nal-01	7:12	33	6.81	
Nal-03	7:58	77	16.06	

REACT-04				
Nal-05	12:14	20	4.50	
Nal-07	20:54	14.4	4.11	
Nal-08	6:41	333	65.25	
Nal-13	7:59	203	40.7	
Nal-21	16:07	20	5.67	

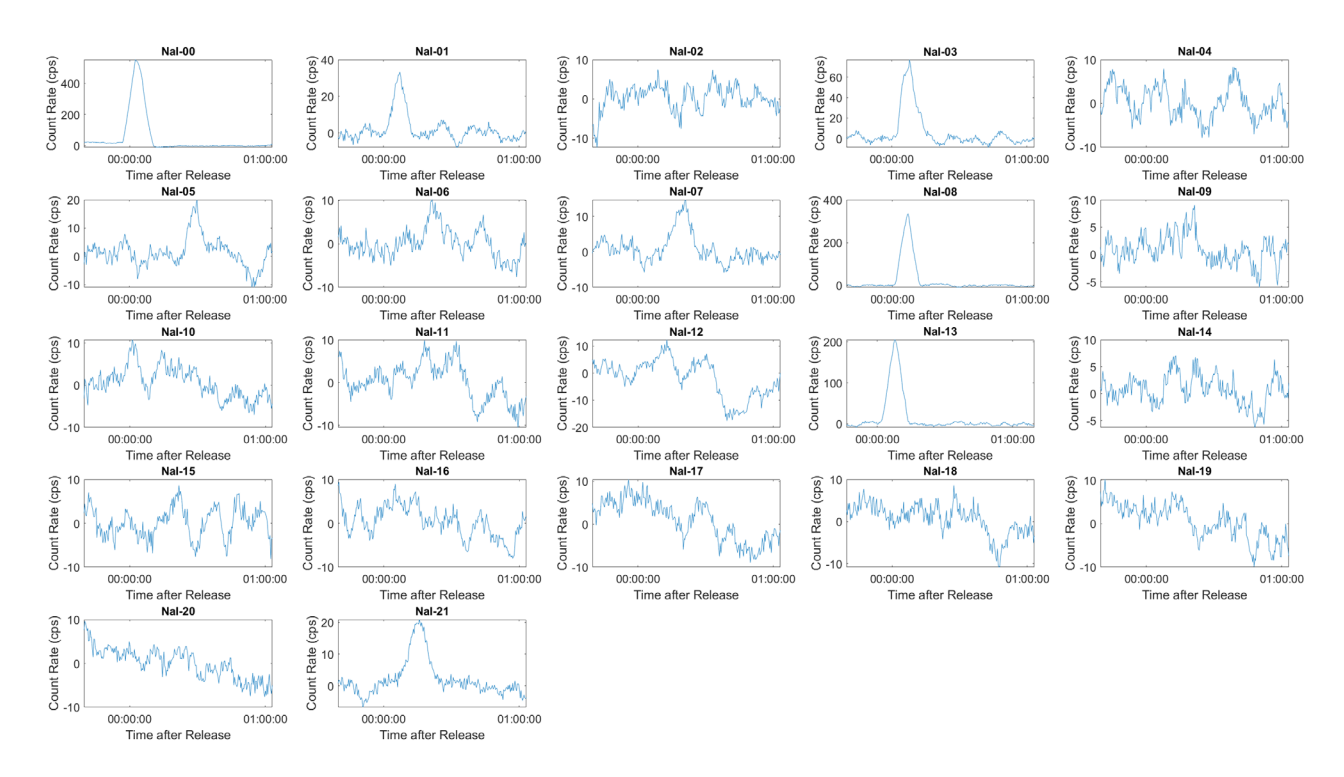


Figure 12: The background subtraction procedure described in Section 2.2 applied to REACT-04. Count rates are for the Xe-127 ROI region from 20 to 220 keV. Nal-00, Nal-01, Nal-03, Nal-08, Nal-13, and Nal-21 made detections.

2.4 Synthetic Data Studies

Synthetic data were used to explore the extent to which real data would be affected by the various summing procedures and inclusion of noise. The goal of these synthetic data studies was to improve the detection ability and to understand the effect of the chosen numerical procedures on the raw data. Other smoothing techniques can be investigated and incorporated as follow on work. The current techniques appear to be sufficient to determine the detection timing and amount above background. This section summarizes the synthetic data studies and the size of the timing and smoothing effects.

2.4.1 Spectra Summing Effect on Timing

Spectra summing was incorporated to improve counting statistics and improve the ability to discern a possible detection compared to noise in the data. Measurements were taken every 20 seconds to provide reasonable sampling to see changes in counts. However, 20 seconds does

not provide a reasonable count time to see noticeable count changes when the activity of the species is small. To improve detection, spectra were summed forward in time to obtain a longer count. This resulted in timing effects such as artificially shifting detection events earlier in time, and causing the duration of a detection event to increase. Spectra were summed from 1 minute up to 6 minutes. A running spectra sum resulting in 5 minutes was chosen as the highest count time without overwhelming detection events with additional background counts.

Implementing spectra summing and background subtraction introduces a timing offset in the final data output. The effect of summing spectra forward in time has two observable effects. The first is "moving the counts backward in time," as counts are added from subsequent acquisitions to the current spectrum. The second is increasing the width of a possible detection event. This occurs because the increased count rate is being added across the number of summed spectra. When the number of spectra being summed is larger than the time of the presence of the radioactive source, then the total count rate decreases. This is due to the lower background count being added to the summed total.

To illustrate these effects, assume the count rate increases for 10 measurement iterations due to the presence of a radioactive source. Then, summing forward in time five iterations will cause the detection to appear five iterations earlier. In addition, summing forward in time by 10 iterations will cause the detection to appear 10 iterations before. A second consequence is that the detection event width will increase when a running sum is applied. The width increases by one iteration less than the number of summed spectra. This gives an empirical formula of $S_w = n + (s-1)$ with S_w as the new width, n as the original width, and s as the number of summed spectra. The effect is illustrated in Figure 13, which shows a synthetic detection summed for a different number of iterations. Then, when spectra are summed beyond the detection width, the initial peak height will decrease. The area under the detection event was calculated for different numbers of summed spectra and no change was observed between summed spectra. The area is preserved for summing, while the peak height and width are not.

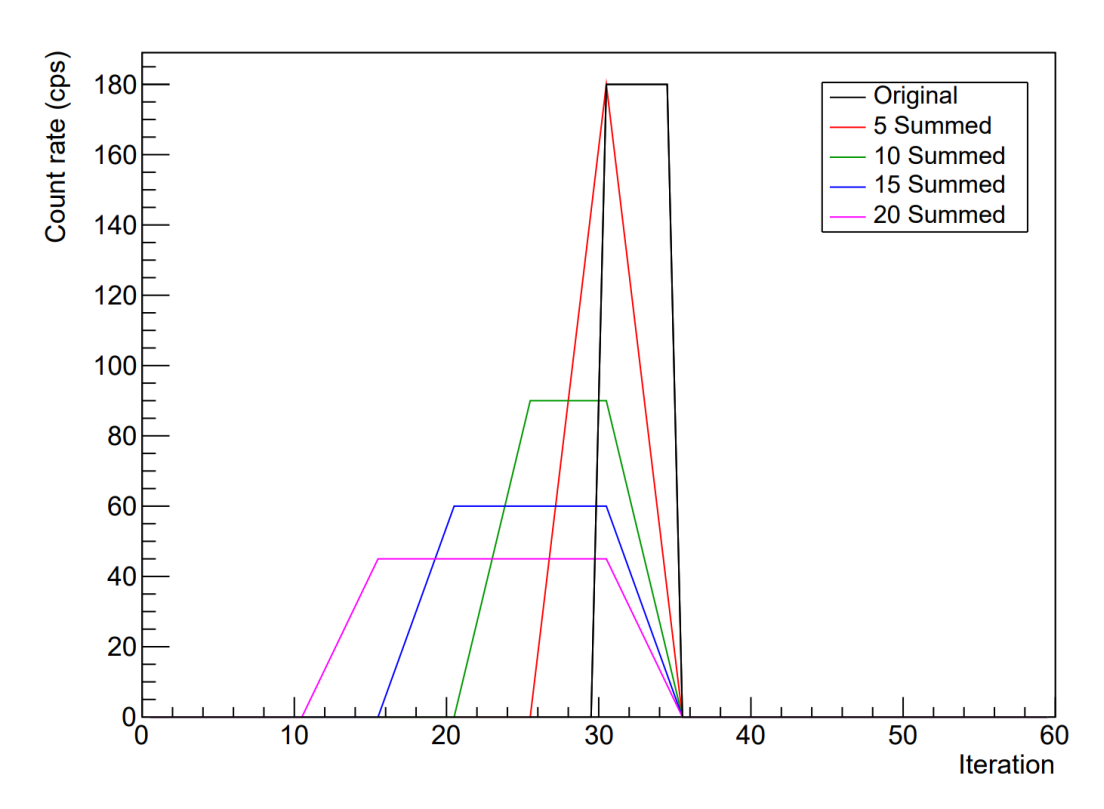


Figure 13: Artificial detection created to demonstrate the effect of summing spectra. Summing spectra shifts the start of the count increase for a detection, causes the detection width to widen, and the height to decrease.

Spectra were summed to improve the likelihood of identifying a possible detection. The summing would shift the start of the detection event backward in time due to the forward summing. This was easily corrected by shifting the summed spectra forward by the offset time. In addition, the summing would elongate the duration of the detection event. This effect was noticed, but further analysis and methods to correct for this were not investigated. Subsequently, investigating the duration of detection events was not part of this study.

2.4.2 Synthetic Data Injected with Noise Performance

A sensitivity study was performed using synthetic data and Poisson distributed random background counts to better understand the limits of detection using this analysis process. Synthetic data was created, and noise was injected to the signal to test and demonstrate the background subtraction procedure. A synthetic signal was created by copying a background spectrum and a spectrum with a radioxenon detection. The spectrum with a radioxenon detection was placed at different positions and with different widths in conjunction with the background spectrum. An example of the synthetic data without noise is shown in Figure 14.

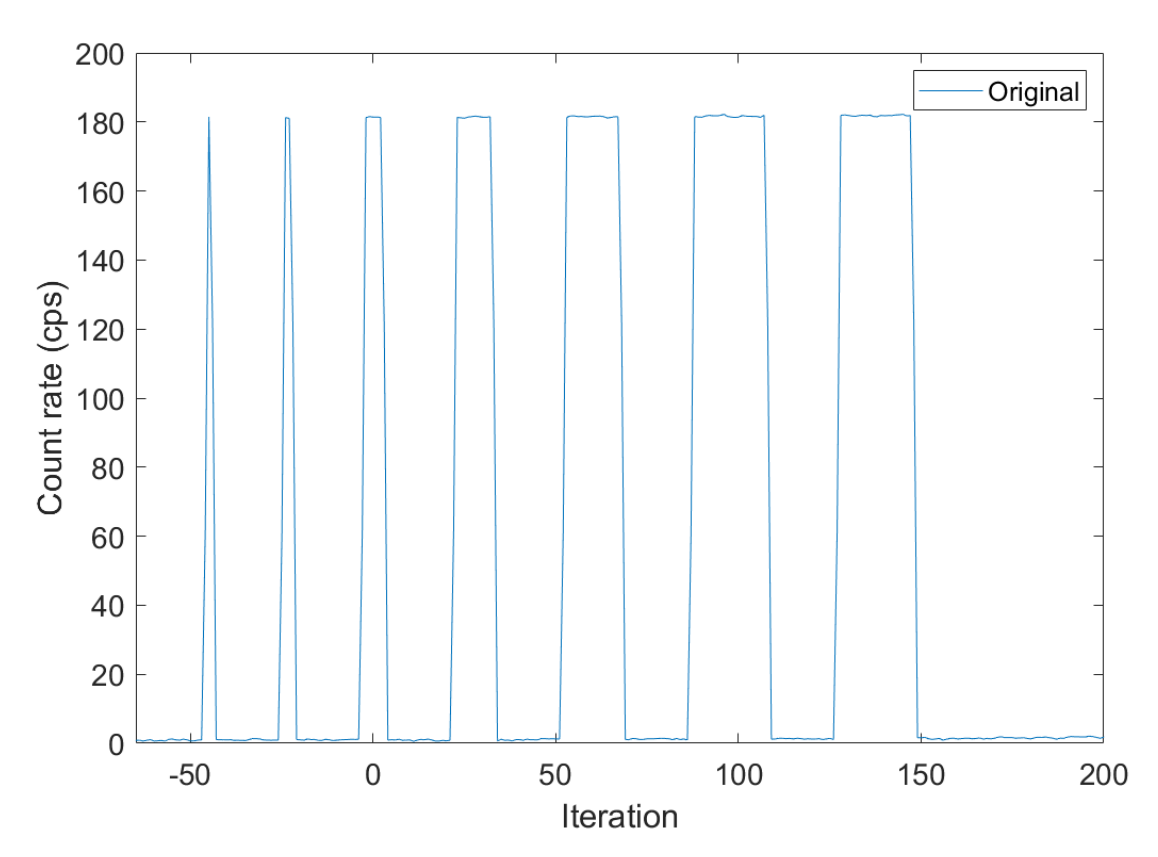


Figure 14: Synthetic detection signal consisting of different widths created from a background spectrum and a spectrum with a radioxenon detection.

MATLAB's poissrnd() function was used to inject Poisson noise into the signal. Noise was introduced by adding a random signal produced by the poissrnd() function to each background spectrum. The rate parameter can be adjusted to increase the amount of noise present in the signal. The rate parameter specifies the average number of events in a time interval to be used by the poissrnd() function. Subsequently, the spacing of the detection events in Figure 14 was increased to prevent the detection from being summed together and is illustrated in Figure 15 and Figure 16.

First, the injected noise is low with a rate parameter of 2. The detection signals are still easily observed when injected with this amount of noise. From Figure 15, it becomes apparent that when summing spectra greater than the width of the detection, the peak height will decrease. This causes the first detection, which is only one iteration wide, to decrease to just above background levels after summing 15 spectra.

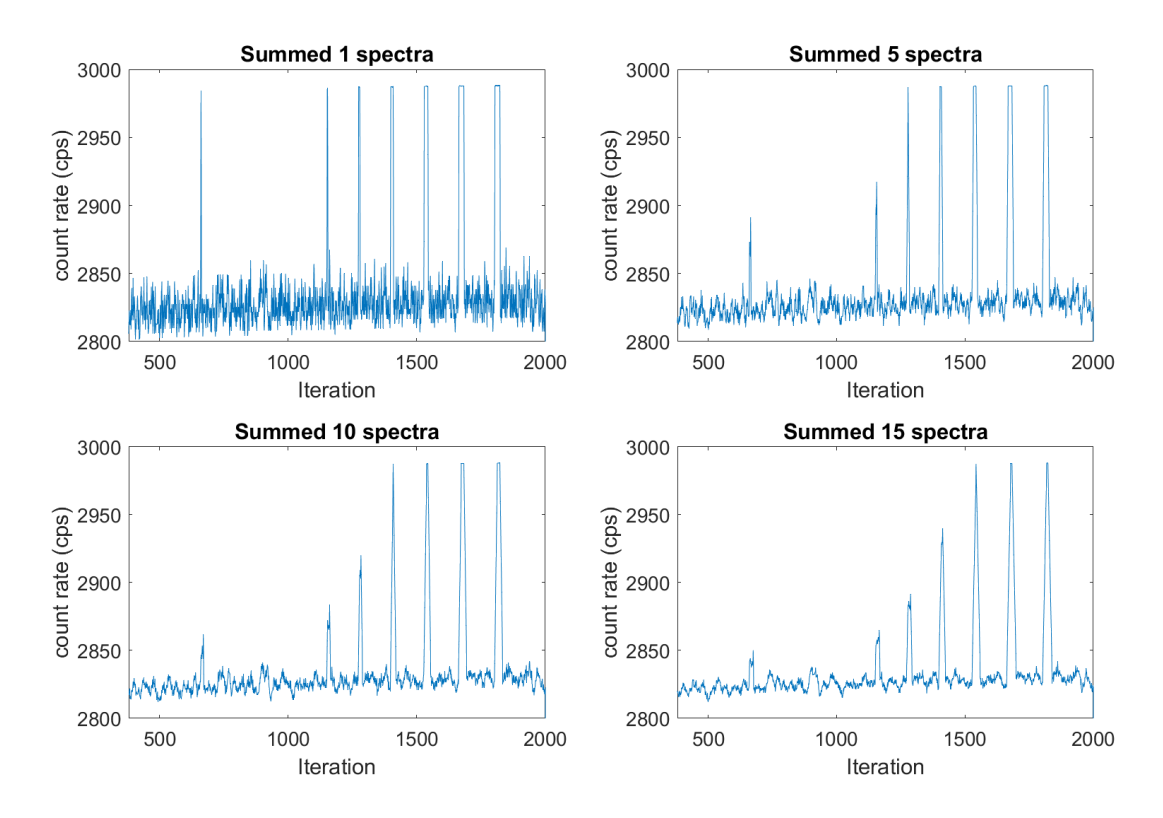


Figure 15: Synthetic signal with a low amount of noise injected. The detections are easy to see, and summing the spectra smooths the detections.

In the second case, the injected noise is increased so the noise is comparable to the synthetic signal using a rate parameter of 12, and the results are displayed in Figure 16. In this case, the summing of spectra helps reduce the background and make the synthetic detection more observable. However, similar to the real dataset, summing spectra introduces a random walk or fluctuation that can create peaks in the series. In conjunction with the decrease in the height of a detection when over-summing the ability to discriminate between noise and a detection can become difficult.

When the detection width is large with respect to the spectra summing, the detections become resolvable even though the signal is buried in noise. In other words, if the detection is long enough in time, spectra summing can resolve the peak. Therefore, the first two synthetic detections are lost during the spectra summing procedure, while the rest of the synthetic detections are not.

These study results helped to confirm the choice of running sum time for the analysis (making it 300 seconds, the same as the duration of the radiotracer releases) and helped to confirm that the timing corrections used were correct.

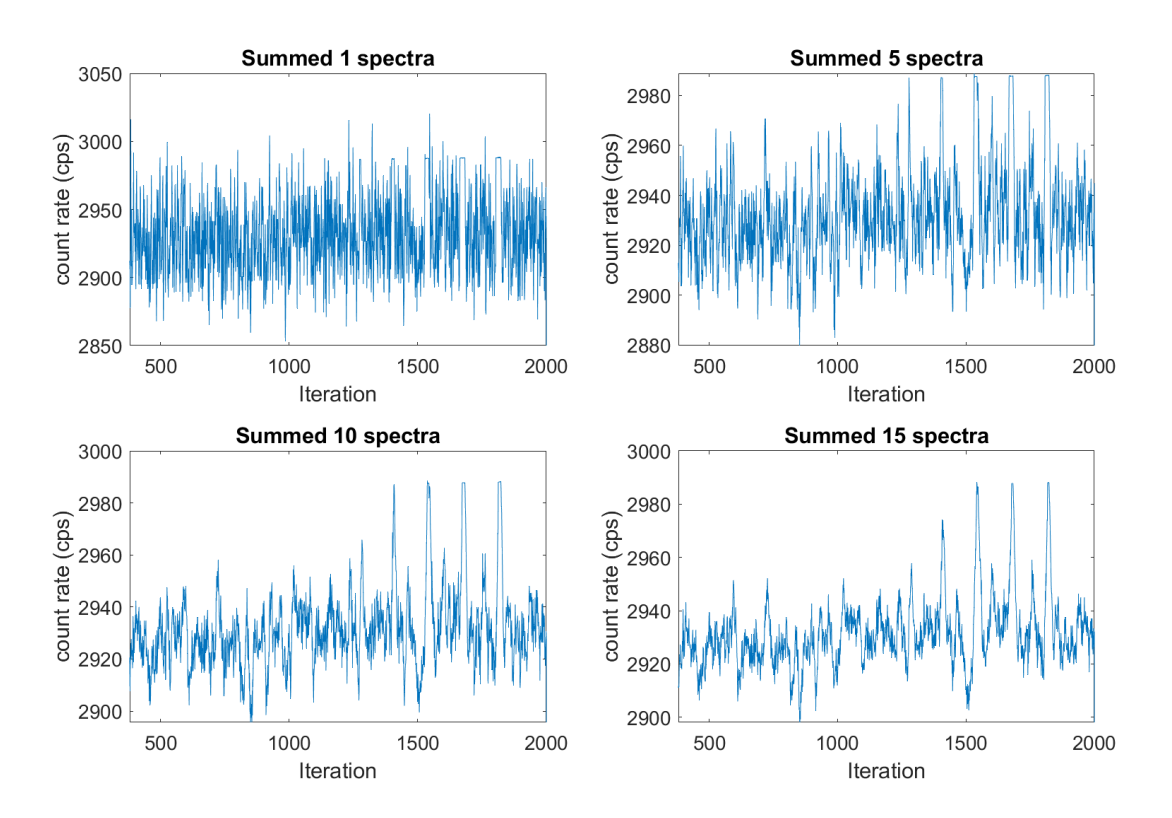


Figure 16: Synthetic signal with a high amount of noise injected. The detections are difficult to see when analyzing the initial signal. Summing the spectra smooths the detection, making the detection more apparent. In addition, summing a random signal creates a random fluctuation.

2.5 Spectral Anomaly Detection Method

As a cross-check on the analysis, an independent algorithm was applied to the data to see if there were any missed detections. The Nuisance-Rejection Spectral Comparison Ratio (NSCRAD) (Pfund, Runkle, Anderson, & Jarman, 2007) algorithm was applied to the REACT-04 data. The NSCRAD algorithm is good at determining if a statistically significant signal is present when a relatively large background signal is present. NSCRAD bins an energy spectrum into various, optimized windows and looks for differences in the spectral shape. The energy windows were optimized for Xe-127 detection using a known source and representative background. Spectra were integrated over the same five-minute running sum windows that were used in the analysis presented above. The results of NSCRAD were then examined to see when anomalies were indicated and how significant they were.

For the REACT-04 release, this analysis using NSCRAD identified the larger detections for Nal-00, Nal-03, Nal-08, and Nal-13 at similar times as shown in Table 5 above. NSCRAD indicated weaker detections for Nal-01 and Nal-07 also at similar times to Table 5. However, NSCRAD did not indicate anomalies for Nal-05 and Nal-21 near the times listed above. There were some clusters of higher NSCRAD metric values near the indicated detection times but they were not above the NSCRAD threshold.

No other detectors had NSCRAD results above threshold within an hour after the REACT-04 release. However, the results for NaI-05 and NaI-21 indicate that with some additional

optimization, there could be more positive detections using the NSCRAD algorithm. But, NSCRAD will also be facing the same challenges presented by small signals as the previous analysis. In that case, it is difficult to determine what is a statistically significant detection above the time varying background.

3.0 Nal Detector Relative Peak Efficiencies

In this section, the methods used to calculate relative peak efficiencies for the detection of Cesium-137 (Cs-137) using 2"×4"×16" Nal detectors with an optically coupled photomultiplier tube and attached Osprey multichannel analyzer are described.

3.1 Methodology

Twenty-two detectors numbered NaI-00 to NaI-21 were used to collect 1,100 gamma spectra of the same Cs-137 source in the field at the Nevada National Security Site (NNSS). The goal of the field measurements was to verify an acceptable energy resolution for each system before deploying around the NNSS. The precise geometry of the measurement was not as carefully controlled as in the laboratory measurements shown in a later section. However, the field measurements were useful for confirming the approximate detection efficiency of each system just before deployment. The measurements confirmed that each detector was undamaged and performing properly immediately prior to being deployed.

Roughly speaking, a similarly sized subset of the 1,100 spectra was collected by each detector during the measurements with the Cs-137 source. Each spectrum was collected for 20 seconds, and the source was observed by each detector for several minutes to assure good statistics. In each test, the radioactive source was placed approximately 1 meter away from two different detectors simultaneously, forming a somewhat triangular arrangement. The orientation of one given detector relative to the source was not necessarily that of the others, though the generalities of the arrangement were consistent, as shown in Figure 17. Thus, the measured peak efficiencies were expected to be similar for each detector.

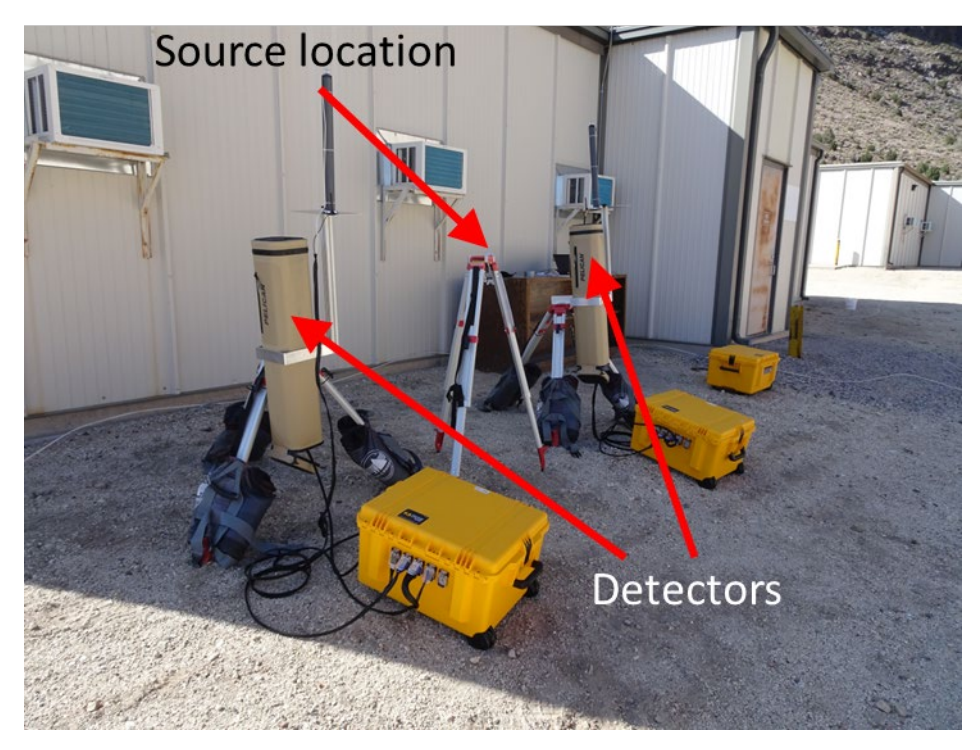


Figure 17: Two real-time xenon sensors undergoing energy calibration and efficiency testing at the NNSS. A Cs-137 source is on the tripod between the two sensors.

To determine the peak efficiency of a given detector, n=14 different spectra from that detector were analyzed except for detectors for which n<14 spectra were collected, in which case n-2 spectra were analyzed (the first and last in a detector-specific set of spectra were neglected). For each spectrum, the Cs-137 peak area was calculated and the uncertainty on that area was estimated. The peak count rate recorded in each spectrum was calculated by dividing the peak area by the detector live time. The average peak count rate from the n spectra and uncertainty on that average were then computed for each detector. The average count rates from the 22 detectors were then divided by that of Nal-00 to obtain a relative measure of the peak detection efficiency.

To locate peaks in the spectra, a rope-filter peak detection algorithm was employed to find the central channel of the Cs-137 photopeak in each spectrum (Winn, 1999). With the relevant peak located in each spectrum, a function was fitted to each peak region that accounts for the essentially Gaussian spread of the photopeak about the peak centroid (Heath, 1997).

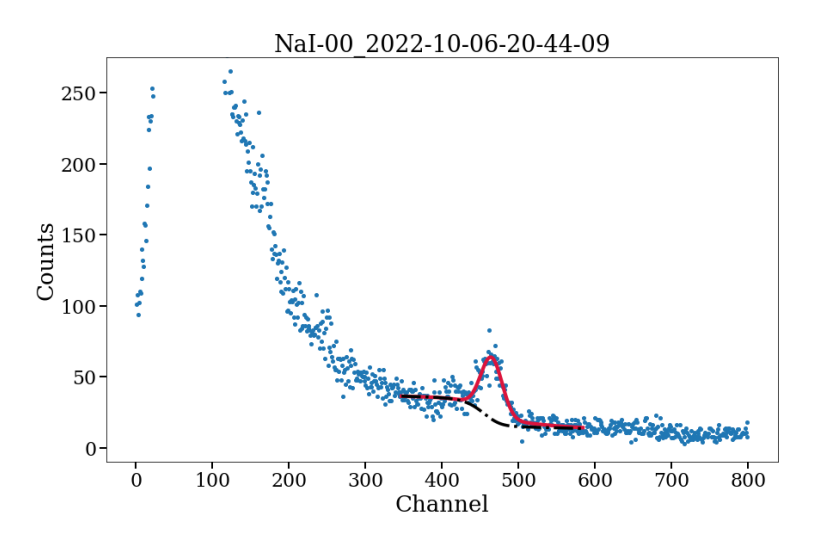


Figure 18: Cs-137 spectrum collected with the Nal-00 detector showing counts versus channels. The photopeak fit function and background curves are shown in the solid crimson line and dot-dashed black lines, respectively.

The fit function was fitted to the data using the nonlinear least-squares method and accounts for various features of the photopeak and background. It is given as

$$f(x) = P_1 e^{-z^2/2} + P_4 \frac{e^{P_5 z}}{(1 + e^z)^4} + \frac{P_6}{(1 + e^z)^2} + P_7 x + P_8,$$

where $z=(x-P_2)/P_3$. The parameter P_1 gives the height of the Gaussian function peak above background, P_2 gives the location of the photopeak centroid, and P_3 gives the standard deviation of the photopeak distribution about P_2 . The second term in the sum on the right-hand side allows for tailing in the peak region at energies below the centroid energy due to incomplete energy deposition, incomplete light collection, and background and absorber effects. The third term on the right-hand side is a tapered step function that allows for a step-like increase in background going from the high-energy side of the peak to the low-energy side, and the final two terms comprise a simple first-order polynomial expression for the background in the vicinity

of the photopeak (Longoria, Naboulsi, Gray, & MacMahon, 1990). An example fit to a spectrum collected with the NaI-00 detector is shown in Figure 18.

Once the function f(x) was fitted to the Cs-137 photopeak, the peak area A was calculated by integrating the fit function minus the background over three and a half sigma centered about the peak centroid P_2 . That is,

$$A = \int_{P_2 - 3.5\sigma}^{P_2 + 3.5\sigma} (f(x) - g(x)) dx,$$

where the background function is

$$g(x) = \frac{P_6}{(1+e^z)^2} + P_7 x + P_8.$$

The parameters P_1 , ..., P_8 were generated during the fitting process for each spectrum, and the integral giving A was computed using Gaussian quadrature. The bounds on the definite integral were selected such that a region equal to three and a half sigma was integrated to give the peak area containing 99.95% of the counts.

The area uncertainty is calculated in a statistical manner rather than by propagating uncertainties on the fit parameters through the area integral calculation for simplicity. This is expected to be a reasonable approximation of the uncertainty on the area estimate. That is,

$$\sigma_A = \sqrt{A + B(1 + n/2m)},$$

where n is the number of channels in the peak region, B is the background area in the peak region, and 2m gives the number of background channels adjacent to the peak region used in the area calculation (Gilmore, 2008). With the area A and uncertainty σ_A calculated for each spectrum of each detector, the peak count rate and uncertainty on that count rate are calculated by dividing A and σ_A , respectively, by the live time T_1 .

In calculating each detector's mean count rate, uncertainty arises due to the variance in area values for the different 20-second spectra included in the calculation of the mean as well as the uncertainty corresponding to each area value. That is, the uncertainty on the count rate, labeled σ_{CR} , is

$$\sigma_{CR} = \sqrt{\sigma_m^2 + \sigma_u^2}$$
 ,

where σ_m^2 is the variance about the mean count rate and σ_u^2 is the contribution from the variances of the individual measurements. The variance σ_m^2 is the square of the sample standard deviation (sample size n as described above) and

$$\sigma_u = \frac{\sqrt{\left(\sum_j \sigma_j^2\right)}}{n},$$

where σ_j is the uncertainty on the count rate calculated from the j^{th} spectrum from a given detector and n is the number of spectra used from that detector.

3.2 Efficiency Results Using Field Data

Once the mean peak count rates and associated uncertainties for each detector were computed, they were divided by the mean peak count rate measured by the Nal-00 detector to obtain a relative measure of the peak efficiency ϵ . That is, for a detector numbered Nal-xx,

$$\epsilon_{\rm rel,xx} = \frac{Act_{\rm NaI-xx}}{Act_{\rm NaI-00}}.$$

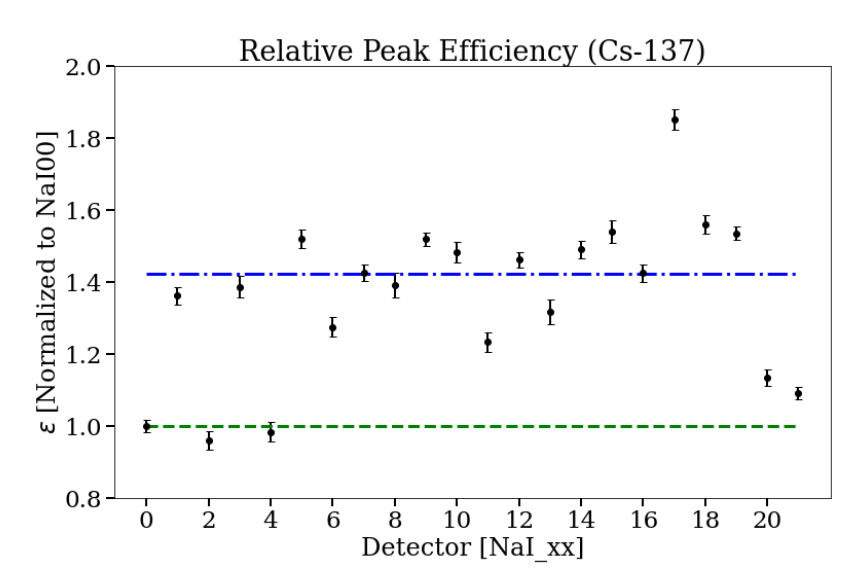


Figure 19: Relative peak efficiency plotted versus detector label. The solid dots correspond to the efficiency values and the error.

The uncertainties on each mean activity were also divided by the mean Cs-137 peak activity of NaI-00. A plot displaying the relative efficiency of each detector versus detector number is shown in Figure 19. In this figure, there appear to be distinct concentrations of relative efficiencies around both 1.0 and slightly above 1.4. The variations in the relative efficiencies are likely explained by changes in the source-detector geometry, including placement of a metal arm holding the detector and where the detector crystal is facing relative to the source. The efficiency values and uncertainties displayed in the figure are also listed numerically in Table 6. As mentioned above, the purpose of these pre-deployment measurements was to verify the detectors were in good working order prior to deployment. The efficiency and energy resolution measurements confirmed this.

Table 6: Relative detector efficiency normalized to detector NaI-00 and the corresponding uncertainty.

Detector	Relative Efficiency	Uncertainty
00	1.000	0.018
01	1.362	0.025

Detector	Relative Efficiency	Uncertainty				
02	0.960	0.025				
03	1.386	0.030				
04	0.984	0.027				
05	1.521	0.026				
06	1.275	0.027				
07	1.425	0.023				
08	1.392	0.033				
09	1.519	0.019				
10	1.483	0.029				
11	1.233	0.026				
12	1.462	0.020				
13	1.318	0.034				
14	1.491	0.024				
15	1.540	0.032				
16	1.425	0.023				
17	1.851	0.029				
18	1.561	0.026				
19	1.536	0.020				
20	1.135	0.022				
21	1.092	0.018				

In Figure 19, detector Nal-17 is somewhat of an outlier, while many detectors, such as Nal-15, have relative efficiencies lying along the upper dot-dashed horizontal trend line. Visual inspection of the spectra from detectors Nal-15 and Nal-17, illustrated in Figure 20, shows that each of these spectra have areas exceeding that of Nal-00 and that the area of Nal-17 exceeds that of Nal-15. Note that the vertical and horizontal scales in each of the two panels of the figure are identical.

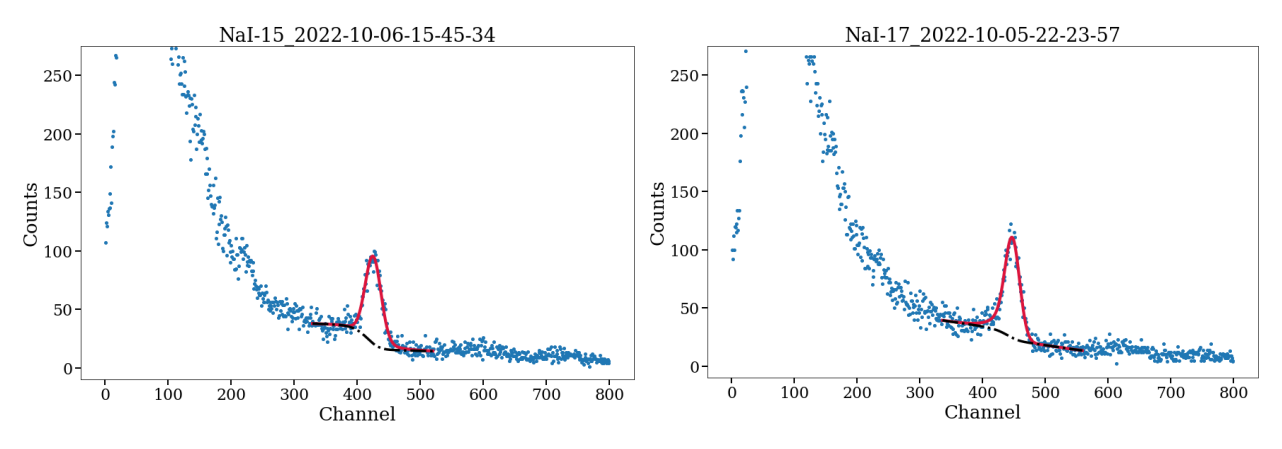


Figure 20: A comparison of typical spectra from detectors NaI-15 and NaI-17 shows that the latter consistently has a slightly larger peak area (2673 counts vs. 2198 counts), while both have a larger peak area than NaI-00 (1632 counts) shown in Figure 18. Greater areas correspond to greater peak efficiencies for equal live times for measurements of the same source activity, assuming the source to detector distance was the same.

In each spectrum, the tailing on the left-hand side of the photopeak was accounted for, while possible tailing on the right-hand side was not. The left-hand side of the photopeak can be greatly influenced by detector shielding (Heath, 1997). In one instance during detector field testing, the Cs-137 source was moved near the detector to observe the 32 keV X-ray peak. Additionally, spectra for many of the bare detectors (i.e., not in their outer casing) were collected with the detectors in a laboratory setting.

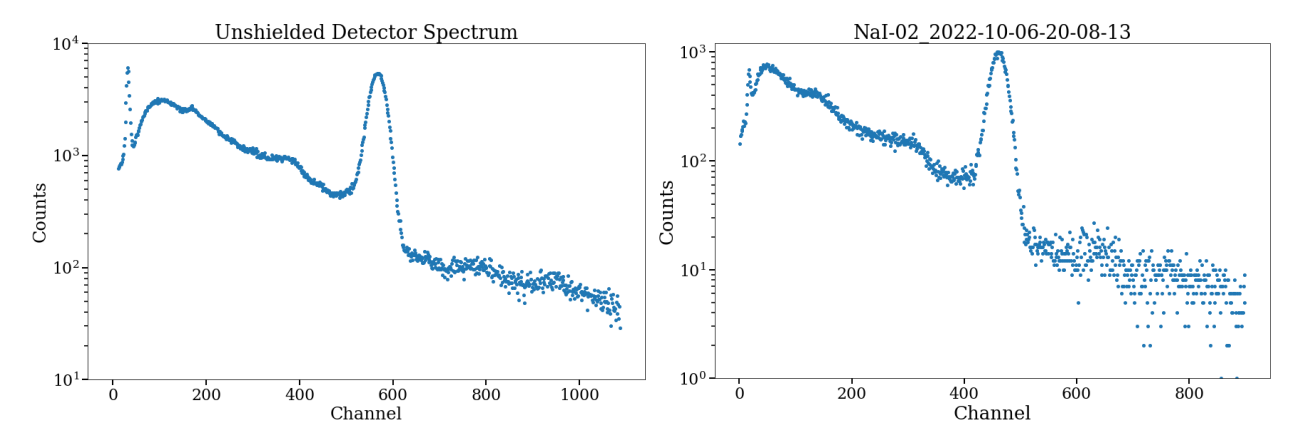


Figure 21: The left figure is an unshielded spectrum taken with the NaI-01 detector. The 32 keV X-ray is more prominent in the unshielded spectrum than in that shown at right taken with NaI-02 in a shielded configuration with the source just outside of the shielding. The vertical axis is logarithmically scaled in each spectrum.

In Figure 21, a spectrum from an unshielded detector and one from a field measurement are compared side by side. The live times are not necessarily the same, but one may draw some conclusions about the attenuation effects of the casing material by comparing the nature of these spectra. As seen in the narrow peak just above Channel 0 in each spectrum, the X-ray peak is attenuated somewhat by the casing material covering the NaI-02 detector in the right-hand spectrum, compared to the bare detector spectrum in the left-hand panel of the figure. A Compton edge for the 661.7 keV peak may be observed in each spectrum a little below Channel 400 on the horizontal scales. In each case, detailed analysis showed that the left-hand side of the photopeak deviates from a Gaussian shape more quickly than the right-hand side, justifying the neglect of tailing on the right-hand side of the photopeak in the fit function f(x) given above.

3.3 Efficiency Results Using Laboratory Data

While the geometry was not closely controlled in the field trials and the corresponding relative efficiencies varied significantly, a comparison with laboratory trials taken for 20 of the detectors was conducted. A spectrum was collected for each detector with live times just under 600 seconds. From these spectra, the peak count rates were calculated and normalized to a peak count rate of 290 counts per second, i.e., a simulated count rate. The peak count rates are plotted in Figure 22, and the corresponding relative efficiencies are plotted in Figure 23. The relative efficiencies still vary about 1.0, and importantly, the standard deviations on the values are quite small. The dot-dashed line at $\epsilon=1$ in Figure 23 is outside of 2σ for nearly two thirds of the detectors, where σ is the uncertainty on a given detector's measured relative efficiency. The measurements were not taken strictly with the goal of getting exact data on Cs-137 peak efficiency, so it is not clear if the slight variations in relative efficiencies can be accounted for by other small, systematic variations in the measurement process.

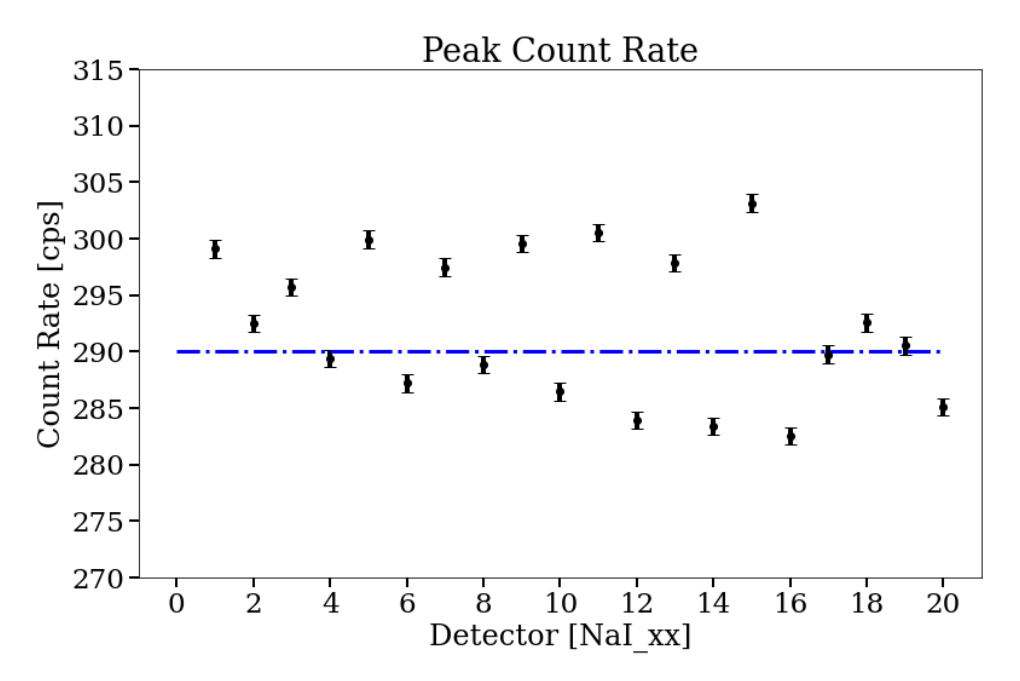


Figure 22: Peak count rate shown by the detectors. Note that only detectors NaI-01 through NaI-20 were tested in this fashion. The peak count rates vary about the expected value of 290 cps. Also note the suppressed zero on the y axis.

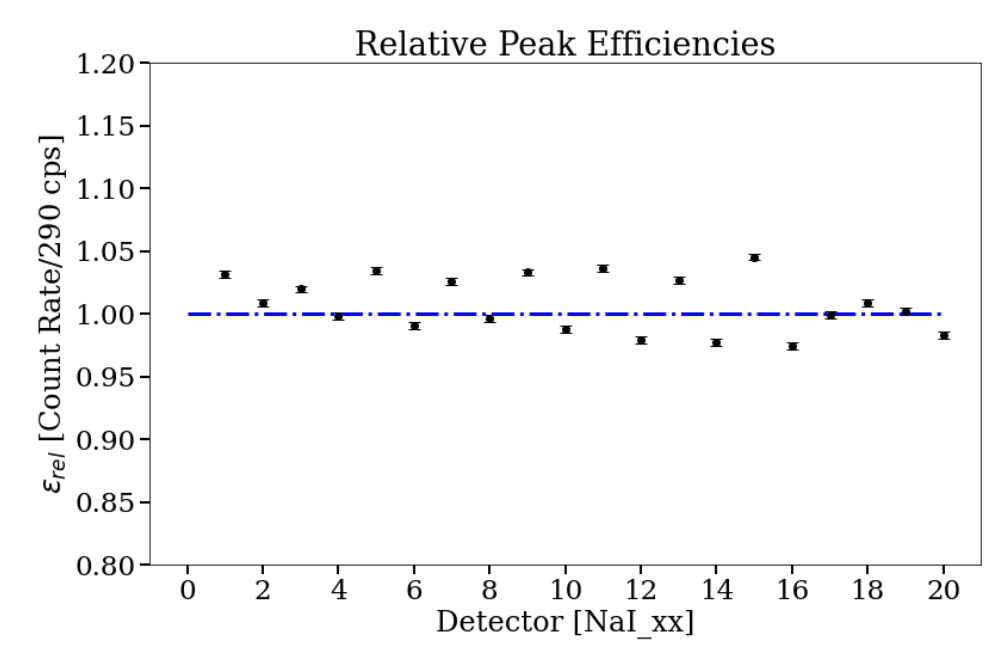


Figure 23: The relative peak efficiencies are obtained by dividing each peak count rate and uncertainty by the expected value of 290 cps. The resulting relative measures of efficiency show a greater consistency than the efficiencies plotted in Figure 19. Note the suppressed zero on the y axis.

3.4 Efficiency Analysis Summary

In summary, to determine the relative detector efficiencies more carefully, it would be helpful to collect or compare spectra that were collected with the detector in a more consistent geometrical arrangement with respect to the source that is specifically designed to obtain good efficiency data. Nevertheless, many of the detectors were in reasonable agreement with each other despite the variations in the source-detector geometry associated with the relative efficiencies of Figure 19. The agreement was greatly improved when the geometry had a greater degree of consistency, as evident in Figure 23. Further studies could determine if the detectors have statistically significant differences in peak efficiencies.

4.0 Updated Detector Response Voxels

The initial simulated real-time xenon sensor detector responses relied on a single-volume, 300 meter radius, hemi-spherical or cylindrical Xe-127 source. The volume was filled with air and had realistic soil about 1 meter thick on the ground. A validated sodium iodide detector model was also used. The geometries were set up in Monte-Carlo N-Particle (MCNP) (6.2 MCNP6 Version 2.0 User's Manual- Code Version, 2017), and this method captures all the scattering and attenuation that would be expected in a real system.

However, the initial simulations were of a homogeneous Xe-127 source. From the initial meteorological modeling results, such monolithic sources are not expected during measurement campaigns. The concentrations will vary on distance scales smaller than the 300 meter radius dome. The first attempt to have a more accurate detector response broke the 300×300×300 meter Quadrant (see Figure 24 for a summary of the geometry) into 27 100×100×100 m voxels (a voxel is the three dimensional analog to the two dimensional pixel used in images). Due to the detector geometry, only one quarter of the space needs to be simulated with active voxel sources (simulated one voxel at a time). The other quadrants are present in the model as air. The detector response to voxels in other quadrants can be reproduced by the appropriately chosen voxel from Quadrant 1 (assuming the ground is flat over the 600× 600 meter region). A physics-informed interpolation routine was used to determine the detector response to voxels smaller than 100 meters. These smaller, interpolated voxels were combined with predictions from meteorological models (see Section 5.0) to give predicted detector responses versus time.

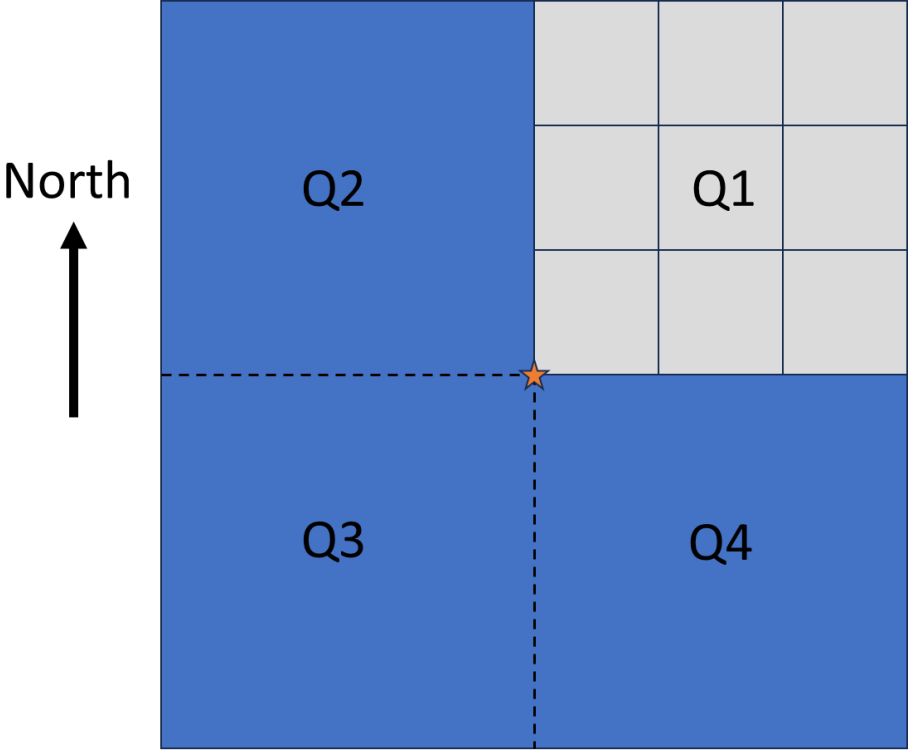


Figure 24. Top-view diagram of the symmetric quadrants around the central detector (star) that were used for the 100 meter voxels (Q1, upper right quadrant). The Qs refer to the quadrant number.

However, there was concern about the accuracy of the interpolation in the nearby (\sim 100 m) region because the voxels were relatively large compared to the attenuation length of the relevant gamma rays. A new set of 64 smaller, $20\times20\times20$ m voxels was then generated that covered part of the region of Quadrant 1 out to 80 m. Figure 25 compares the original and new detector response voxels centered at X = 10 m. The upper-left plot is the closest voxel, and the new response has much more spectral structure, as would be expected in experimental measurements. The relative strength of the original and updated voxels varies with distance. However, the new voxels should be more accurate since there is no interpolation being applied. These new voxels were then used for the results shown in Section 5.0.

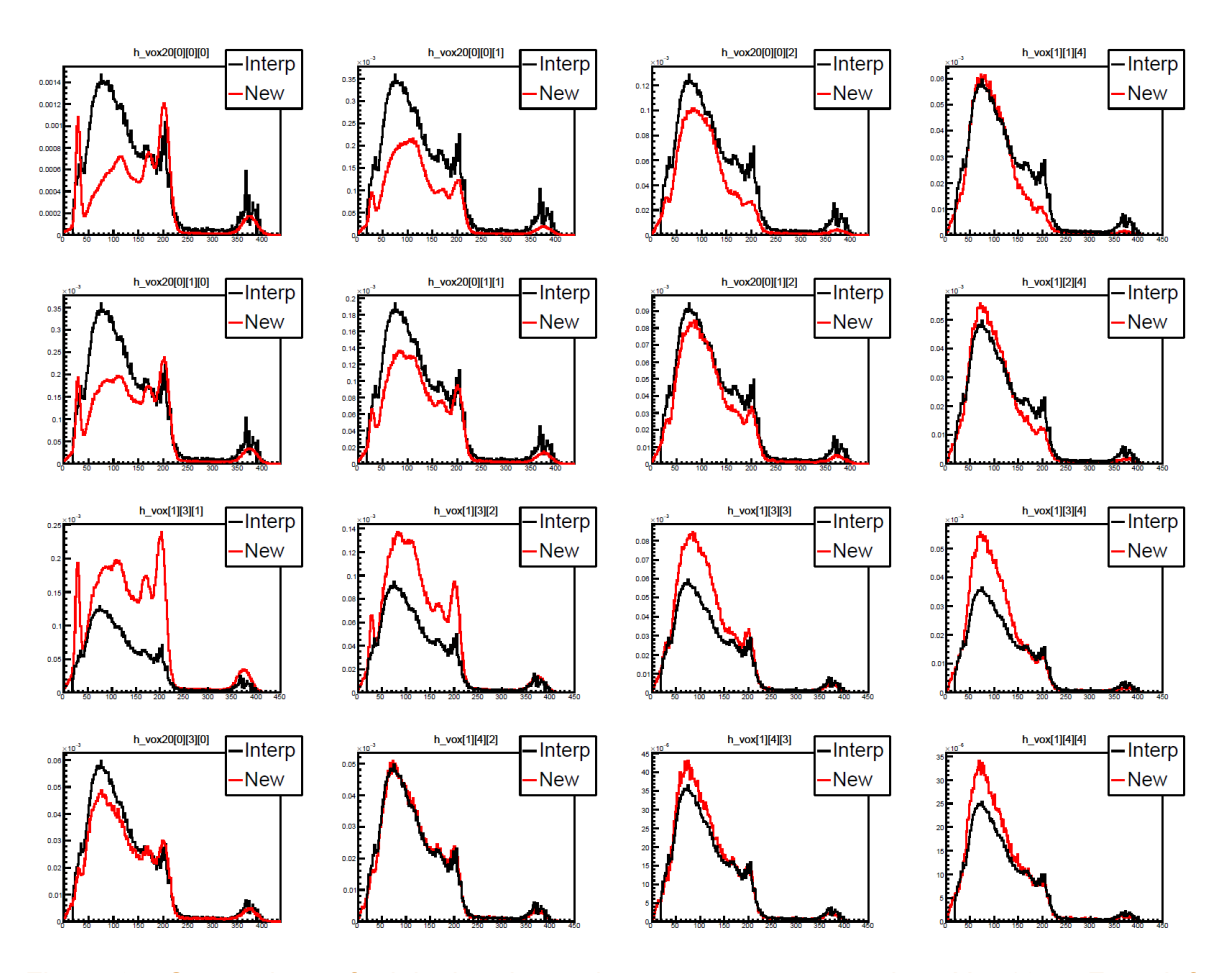


Figure 25: Comparison of original and new detector response voxels at X = 10 m. From left to right is steps in z of 20 m centered at 10, 30, 50, and 70 m. Top to bottom is steps in y of 20 m centered at 10, 30, 50, and 70 m.

5.0 Comparison of Experimental Data with Meteorological Modeling Results

The results of two different meteorological models (detailed below) were compared with the measured REACT-04 data. Both models provide predictions of dilution factors versus time on a fine grid. The predicted dilution factors from the models were then averaged over the voxel size (either 20×20×20 m for nearby voxels or 100×100×100 m for the distant voxels). A small region between 80 and 100 m was not included (the 20 meter wide difference between an 80×80×80 meter cube and a 100×100×100 meter cube that share a corner), leading to an expected underestimated effect in some cases of up to 10% (the relative amount of radiotracer in the region was logged to verify it was a small amount). This region will be filled in when the 40×40×40 m voxels between 80 and 200 m are available in fiscal year (FY) 2024. Note that this is an initial comparison for both meteorological models. Some iterations were already performed on one of the models. Additional iterations and parameter studies are planned for both models in FY24.

5.1 FLEXPART-WRF

FLEXPART-WRF (Brioude, et al., 2013) is a Lagrangian particle dispersion model. The terrain from around the release location was used along with the measured meteorological data for the release day and time for REACT-04. The wind speed on the P-Tunnel apron was 6.3 m/s, out of 6 degrees north, and the conditions were stable. Only REACT-04 has been examined in detail up to this point because REACT-04 has the most detections that could be used for comparison. Combining the FLEXPART-WRF calculations with the updated detector response voxels gives the results shown in Figure 26. The magnitudes agree for some detections, but the timing and locations match up well even if the magnitude differs. Additional refinement and iterations are expected in FY 2024.

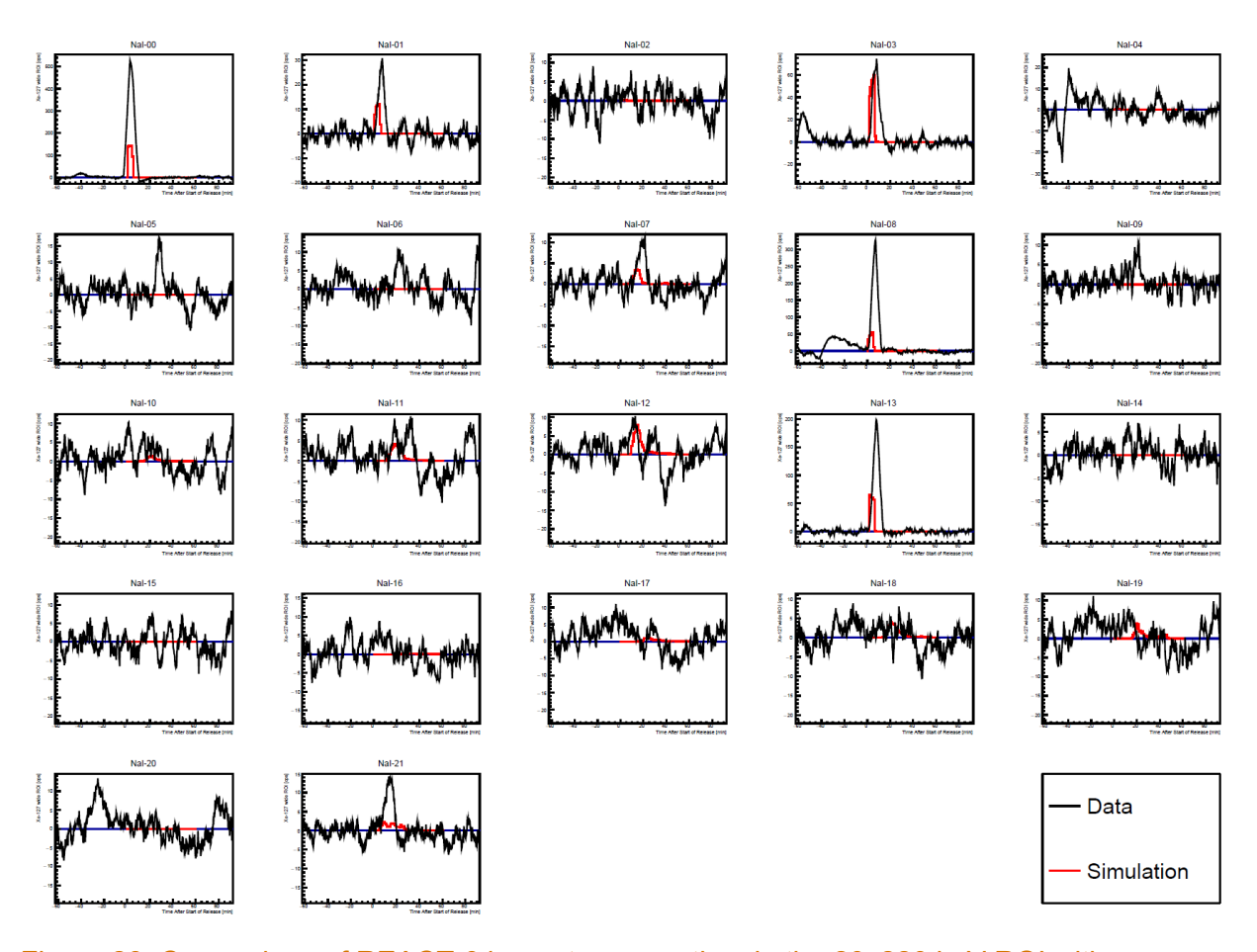


Figure 26: Comparison of REACT-04 counts versus time in the 20–220 keV ROI with FLEXPART-WRF calculations for 6.3 m/s, 6 degrees, and stable conditions.

5.2 Aeolus

The Aeolus meteorological model (Gowardhan, et al., 2021) has been developed by Lawrence Livermore National Laboratory and is designed for efficient and accurate simulations of local terrain and small feature effects. A copy of the code has been transferred to Pacific Northwest National Laboratory and simulations were performed across a variety of meteorological conditions. The measured conditions for REACT-04 were used as a foundation, and the wind speed, direction, and stability class were then varied in an attempt to find a combination that best matches the measured data. Due to the complexity of the terrain, it is likely not accurate to use the measured results from a single location in the valley. This type of a search may also help determine where the most useful meteorological condition measurements could be made.

After searching through approximately 50 parameter combinations, the results shown in Figure 27 were found. Instead of the measured P-Tunnel apron conditions of 6.3 m/s out of 6 degrees with stable conditions, the best match to the data, so far, was with 4 m/s winds out of 350 degrees under neutral conditions. Note that the simulations were smoothed in the same way that the data were smoothed for a fair comparison. The effect is not large but will also be applied to the FLEXPART-WRF calculations in FY 2024.

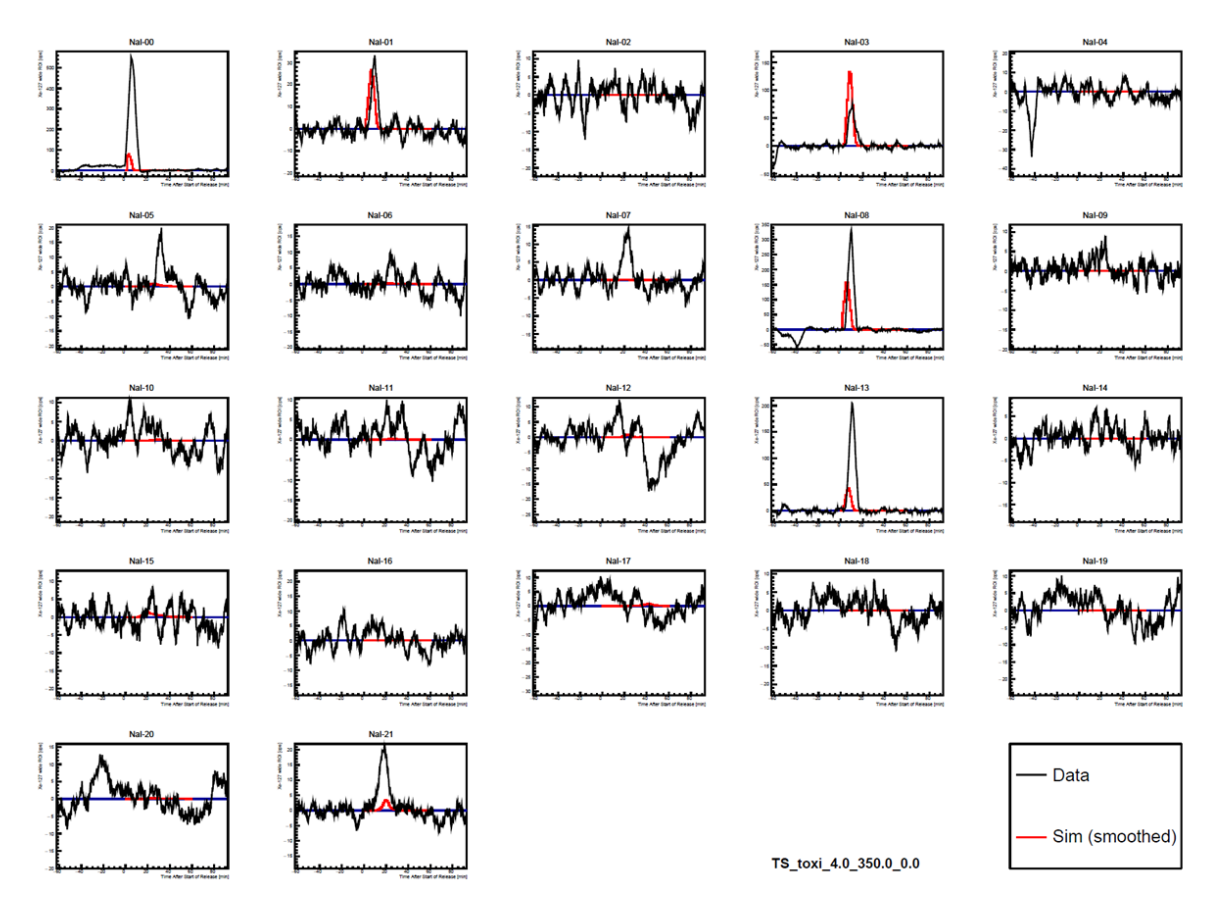


Figure 27: Comparison of REACT-04 counts versus time in the 20–220 keV ROI with Aeolus calculations for 4 m/s, 350 degrees, and neutral conditions.

The results are encouraging, and the analysis team is planning to meet with the meteorological modelers to determine next steps.

5.3 Discussion

For both models, the rolling five-minute sum of background subtracted counts is plotted minute by minute. The timing offsets introduced by the time window have been accounted for. While the exact start time of the detection gets washed out in this analysis, if the beginning and end of detection agree between the model and data, then the model and data are indicating agreement on start time and duration. The data and model outputs have both been transformed in the same way so they can be compared. The team has not yet looked at other methods that would preserve the timing information while also maximizing the signal to noise ratio.

The duration of the radiotracer plume is expected to increase for detectors located farther from the release point. However, many factors affect how the signal appears in the detectors. If the plume arrives but is at higher heights above the ground, its increased distance from the detector will lower the counts collected. The plume would need to be at relatively high concentrations near the ground to be detected. The farthest out near-detect observed was for NaI-07 which was about 2 km from the release point. There, the duration of the plume in the processed/smoothed data was slightly longer at ~16 minutes, versus the ~11 to ~14 minutes observed at closer-in detectors. Had there been positive detections at the 3.5 or 4.5 km arcs,

perhaps an even longer plume duration would have been observed. The studies on the plume duration could be a possible topic to study in the next fiscal year.	

6.0 Summary and Future Work

The original real-time xenon sensor data collected in October 2022 during the REACT-01 through -04 releases was analyzed in more detail in FY 2024. Improved offline gain stabilization using the temperature peak-shift correction technique was applied along with an improved background subtraction routine (exponentially weighted moving average). The relative detection efficiency for each sensor was measured in the laboratory and in the field. The in-field measurements were originally intended as a final check that the system was performing as expected after being transported to the NNSS and then moved for assembly. Those measurements showed that the systems were performing as expected. Laboratory measurements conducted before the field deployment verified that the systems all had very similar efficiencies.

The updated analysis results were then compared against updated detector response models coupled with two meteorological model calculations based on the conditions of REACT-04. Both models were able to achieve some level of agreement on the timing and location of positive detections. Some detections matched in magnitude, and all the negative detections agreed.

The presented results were achieved at the end of the fiscal year. The real-time xenon sensor analysis team plans to meet with both MET modeling teams to iterate and see what additional improvements may be possible. The results from REACT-03 then REACT-01 and REACT-02 will also need to be examined. While there were a lower number of detections for those releases, a comparison between the models and the measured weather conditions that led to those detections would still be of value.

7.0 References

- 6.2 MCNP6 Version 2.0 User's Manual- Code Version. (2017). *LA-UR-17-29981*. Los Alamos, New Mexico: Los Alamos National Laboratory.
- Box, G. E., Luceno, A., & del Carmen Paniagua-Quinones, M. (2011). *Statistical control by monitoring and adjustment*. John Wiley & Sons.
- Brioude, J., Arnold, D., Stohl, A., Cassiani, M., Morton, D., Seibert, P., . . . Wotawa, G. (2013). The Lagrangian particle dispersion model FLEXPART-WRF VERSION 2.1. *Geosci. Model Dev.*, *6*, 1889-1904.
- Casanovas, R., Morant, J., & Salvado, M. (2012). Temperature peak-shift correction methods for NaI (TI) and LaBr3 (Ce) gamma-ray spectrum stabilisation. *Radiation Measurements*, 47(8), 588-595.
- DeGeer, L.-E. (2004). Currie detection limits in gamma-ray spectroscopy. *Applied Radiation and Isotopes*, 151-160.
- Gilmore, G. R. (2008). Statistics of Counting. In G. R. Gilmore, *Practical Gamma-Ray Spectrometry* (pp. 101-129). John Wiley & Sons, Ltd.
- Gowardhan, A. A., McGuffin, D. L., Lucas, D. D., Neuscamman, S. J., Alvarez, O., & Glascoe, L. G. (2021). Large Eddy Simulations of Turbulent and Buoyant Flows in Urban and Complex Terrain Areas Using the Aeolus Model. *Atmosphere*, *12*, 1107.
- Heath, R. (1997). *Scintillation Spectrometry: Gamma-Ray Spectrum Catalogue*. Idaho National Engineering & Environmental Laboratory.
- Longoria, L., Naboulsi, A., Gray, P., & MacMahon, T. (1990). Analytical peak fitting for gammaray spectrum analysis with Ge detectors. *Nuclear Instruments and Methods in Physics Research A*, 308-312.
- Mitra, P. (2016). Application of spectrum shifting methodology to restore NaI (TI)-recorded gamma spectra, shifted due to temperature variations in the environment. *Applied Radiation and Isotopes, 107*, 133-137.
- Pfund, D. M., Runkle, R. C., Anderson, K. K., & Jarman, K. D. (2007). Examination of countstarved gamma spectra using the method of spectral comparison ratios. *IEEE Transactions on Nuclear Science*, *54*(4), 1232-1238.
- Stave, S. C., Zalavadia, M. A., McGaughey, S. D., Santiago, F., Stewart, T. L., Becker, E. M., . . Gowardhan, A. A. (In process). *Real-time Xenon Sensor Design and Performance.*
- Winn, W. G. (1999). GRABGAM: A Gamma Analysis Code for Ultra-Low-Level HPGe Spectra. *Westinghouse Savannah River Company*.

References 44

Appendix A – EWMA Uncertainty Derivation

The uncertainty derivation for exponentially weighted moving average (EWMA) is from (Box, Luceno, & del Carmen Paniagua-Quinones, 2011). First, write out the terms of the EWMA.

$$v_i = (1 - \alpha)r_i + \alpha(1 - \alpha)x_{i-1} + \alpha^2(1 - \alpha)x_{i-2} + \cdots$$

The series can be simplified by pulling out the $(1 - \alpha)$ term.

$$v_i = (1 - \alpha)(r_i + \alpha r_{i-1} + \alpha^2 r_{i-2} + \cdots)$$

The assumption is made that variances are linearly independent observations such that Var(aX + bY) = aVar(X) + bVar(Y).

The variance of each variable can then be taken separately because they are linearly independent.

$$Var(v_i) = (1-\alpha)Var(r_i + \alpha r_{i-1} + \alpha^2 r_{i-2} + \cdots)$$

$$Var(v_i) = (1 - \alpha)Var(r_i) + \alpha Var(r_{i-1}) + \alpha^2 Var(r_{i-2}) + \cdots$$

Next, it can be assumed that the variances of each r_i are the same, so:

$$Var(r_i) = Var(r_{i-1}) = \sigma_r^2$$

This simplifies to:

$$\sigma_v^2 = (1 - \alpha)^2 (1 + \alpha^2 + \alpha^3 + \alpha^4 + \cdots) \sigma_r^2$$

Also, because $|\alpha| < 1$, then:

$$(1 + \alpha^2 + \alpha^4 + \cdots)(1 - \alpha^2) = 1$$

Therefore:

$$\frac{\sigma_v^2}{\sigma_r^2} = \frac{(1-\alpha)^2(1+\alpha^2+\alpha^3+\alpha^4+\cdots)}{(1-\alpha^2)(1+\alpha^2+\alpha^3+\alpha^4+\cdots)}$$

The second term in parentheses cancels out and leaves the first terms, which can be written as

$$\frac{\sigma_v^2}{\sigma_r^2} = \frac{(1-\alpha)^2}{1-\alpha^2} = \frac{(1-\alpha)(1-\alpha)}{(1+\alpha)(1-\alpha)} = \frac{1-\alpha}{1+\alpha}$$

Solving for σ_v gives:

$$\sigma_v = \sqrt{\frac{1-\alpha}{1+\alpha}}\sigma_r$$

Appendix A A.1

Appendix B – Detector Locations

Staff from the Nevada National Security Site/Mission Support Test Services performed detailed Global Positioning System (GPS) surveys of each of the 22 real-time xenon sensors. The tip of the GPS survey meter was placed on the ground below the sensor. Each sensor was mounted so that the center of the crystal was approximately 1 meter above the ground. There are three tables below because some of the detectors were relocated between REACT-02 and REACT-03 and between REACT-03 and REACT-04. Table 7 lists detector locations for REACT-01 and -02. Table 8 shows detector locations for REACT-03. Table 9 shows detector locations for REACT-04.

Table 7: Sensor locations for REACT-01 and REACT-02

Det. Lat. Lon. Northing (m) Easting (m) Elev. (m, GEOID18) Height above ellipsoid Hor. Prec. (m) Vert. Prec. (m) Prec. Dilution Precision Nal-00 37.23034318 -116.15191619 4120762.466 575231.671 1673.718 1647.877 0.016 0.041 1.5	n of
Nal-00 37.23034318 -116.15191619 4120762.466 575231.671 1673.718 1647.877 0.016 0.041 1.5	
Nal-01 37.22847956 -116.15268040 4120555.107 575165.729 1671.790 1645.945 0.018 0.038 1.4	
Nal-02 37.22655223 -116.15419010 4120340.090 575033.710 1734.393 1708.544 0.021 0.041 1.2	
Nal-03 37.22559672 -116.14842828 4120238.666 575545.817 1633.232 1607.385 0.014 0.026 1.1	
Nal-04 37.22802721 -116.14720179 4120509.286 575652.198 1675.379 1649.537 0.014 0.036 1.1	
Nal-05 37.21280132 -116.15347079 4118815.126 575111.158 1603.740 1577.863 0.025 0.035 1.1	
Nal-06 37.21038234 -116.14853845 4118550.685 575551.217 1572.729 1546.846 0.025 0.048 1.2	
Nal-07 37.21138647 -116.14506552 4118664.859 575858.374 1579.540 1553.660 0.014 0.035 1.2	
Nal-08 37.19797620 -116.15427350 4117169.785 575054.613 1585.382 1559.475 0.014 0.027 1.1	
Nal-09 37.19722789 -116.15062831 4117089.661 575378.859 1563.901 1537.989 0.016 0.027 1.0	
Nal-10 37.19890702 -116.14345015 4117281.678 576014.225 1533.834 1507.919 0.019 0.056 1.4	
Nal-11 37.20029156 -116.13989397 4117438.138 576328.430 1530.202 1504.290 0.013 0.022 0.9	
Nal-12 37.20340403 -116.13740935 4117785.442 576545.783 1555.479 1529.576 0.014 0.023 1.1	
Nal-13 37.19140282 -116.16280223 4116433.812 574304.153 1626.028 1600.123 0.024 0.036 1.1	
Nal-14 37.19113808 -116.15543254 4116410.246 574958.512 1591.155 1565.236 0.013 0.031 1.0	
Nal-15 37.19033893 -116.14971998 4116326.121 575466.328 1563.508 1537.580 0.013 0.025 0.9	
Nal-16 37.18885184 -116.14538892 4116164.600 575852.226 1544.889 1518.951 0.021 0.067 1.0	
Nal-17 37.18910314 -116.13851717 4116198.002 576461.897 1518.580 1492.635 0.016 0.031 1.2	
Nal-18 37.19091122 -116.13271366 4116403.288 576975.169 1493.413 1467.467 0.013 0.035 1.2	
Nal-19 37.19251586 -116.12774043 4116585.357 577414.934 1486.600 1460.655 0.014 0.042 1.0	
Nal-20 37.19418066 -116.11980495 4116776.563 578117.525 1496.663 1470.720 0.017 0.021 1.0	
Nal-21 37.22079420 -116.14084997 4119711.944 576222.962 1684.459 1658.610 0.014 0.034 1.2	

Appendix B B.1

Table 8: Sensor locations for REACT-03

Det.	Lat.	Lon.	Northing (m)	Easting (m)	Elev. (m, GEOID18)	Height above ellipsoid	Hor. Prec. (m)	Vert. Prec. (m)	Position Dilution of Precision
Nal- 00_reloc ated	37.22965162	-116.15124936	4120686.274	575291.513	1671.499	1645.657	0.018	0.039	1.3
Nal-01	37.22847956	-116.15268040	4120555.107	575165.729	1671.790	1645.945	0.018	0.038	1.4
Nal-02	37.22655223	-116.15419010	4120340.090	575033.710	1734.393	1708.544	0.021	0.041	1.2
Nal-03	37.22559672	-116.14842828	4120238.666	575545.817	1633.232	1607.385	0.014	0.026	1.1
Nal-04	37.22802721	-116.14720179	4120509.286	575652.198	1675.379	1649.537	0.014	0.036	1.1
Nal-05	37.21280132	-116.15347079	4118815.126	575111.158	1603.740	1577.863	0.025	0.035	1.1
Nal-06	37.21038234	-116.14853845	4118550.685	575551.217	1572.729	1546.846	0.025	0.048	1.2
Nal-07	37.21138647	-116.14506552	4118664.859	575858.374	1579.540	1553.660	0.014	0.035	1.2
Nal-08	37.19797620	-116.15427350	4117169.785	575054.613	1585.382	1559.475	0.014	0.027	1.1
Nal-09	37.19722789	-116.15062831	4117089.661	575378.859	1563.901	1537.989	0.016	0.027	1.0
Nal-10	37.19890702	-116.14345015	4117281.678	576014.225	1533.834	1507.919	0.019	0.056	1.4
Nal-11	37.20029156	-116.13989397	4117438.138	576328.430	1530.202	1504.290	0.013	0.022	0.9
Nal-12	37.20340403	-116.13740935	4117785.442	576545.783	1555.479	1529.576	0.014	0.023	1.1
Nal-13	37.19140282	-116.16280223	4116433.812	574304.153	1626.028	1600.123	0.024	0.036	1.1
Nal-14	37.19113808	-116.15543254	4116410.246	574958.512	1591.155	1565.236	0.013	0.031	1.0
Nal-15	37.19033893	-116.14971998	4116326.121	575466.328	1563.508	1537.580	0.013	0.025	0.9
Nal-16	37.18885184	-116.14538892	4116164.600	575852.226	1544.889	1518.951	0.021	0.067	1.0
Nal-17	37.18910314	-116.13851717	4116198.002	576461.897	1518.580	1492.635	0.016	0.031	1.2
Nal-18	37.19091122	-116.13271366	4116403.288	576975.169	1493.413	1467.467	0.013	0.035	1.2
Nal-19	37.19251586	-116.12774043	4116585.357	577414.934	1486.600	1460.655	0.014	0.042	1.0
Nal-20	37.19418066	-116.11980495	4116776.563	578117.525	1496.663	1470.720	0.017	0.021	1.0
Nal-21	37.22079420	-116.14084997	4119711.944	576222.962	1684.459	1658.610	0.014	0.034	1.2

Appendix B B.2

Table 9: Sensor locations for REACT-04

Det.	Lat.	Lon.	Northing (m)	Easting (m)	Elev. (m, GEOID18)	Height above ellipsoid	Hor. Prec. (m)	Vert. Prec. (m)	Position Dilution of Precision
Nal- 00_reloc ated	37.22965162	-116.15124936	4120686.274	575291.513	1671.499	1645.657	0.018	0.039	1.3
Nal- 01_reloc ated	37.22776673	-116.14933741	4120478.684	575463.002	1650.559	1624.715	0.02	0.043	1.4
Nal-02	37.22655223	-116.15419010	4120340.090	575033.710	1734.393	1708.544	0.021	0.041	1.2
Nal-03	37.22559672	-116.14842828	4120238.666	575545.817	1633.232	1607.385	0.014	0.026	1.1
Nal-04	37.22802721	-116.14720179	4120509.286	575652.198	1675.379	1649.537	0.014	0.036	1.1
Nal-05	37.21280132	-116.15347079	4118815.126	575111.158	1603.740	1577.863	0.025	0.035	1.1
Nal-06	37.21038234	-116.14853845	4118550.685	575551.217	1572.729	1546.846	0.025	0.048	1.2
Nal-07	37.21138647	-116.14506552	4118664.859	575858.374	1579.540	1553.660	0.014	0.035	1.2
Nal- 08_reloc ated	37.22742696	-116.15013517	4120440.354	575392.569	1641.580	1615.735	0.031	0.041	1.2
Nal-09	37.19722789	-116.15062831	4117089.661	575378.859	1563.901	1537.989	0.016	0.027	1.0
Nal-10	37.19890702	-116.14345015	4117281.678	576014.225	1533.834	1507.919	0.019	0.056	1.4
Nal-11	37.20029156	-116.13989397	4117438.138	576328.430	1530.202	1504.290	0.013	0.022	0.9
Nal-12	37.20340403	-116.13740935	4117785.442	576545.783	1555.479	1529.576	0.014	0.023	1.1
Nal- 13_reloc ated	37.22576929	-116.14947506	4120256.977	575452.781	1631.952	1606.104	0.025	0.042	1.2
Nal-14	37.19113808	-116.15543254	4116410.246	574958.512	1591.155	1565.236	0.013	0.031	1.0
Nal- 15_reloc ated	37.21684409	-116.14903548	4119267.159	575500.674	1591.580	1565.712	0.023	0.036	1.1
Nal-16	37.18885184	-116.14538892	4116164.600	575852.226	1544.889	1518.951	0.021	0.067	1.0
Nal-17	37.18910314	-116.13851717	4116198.002	576461.897	1518.580	1492.635	0.016	0.031	1.2
Nal-18	37.19091122	-116.13271366	4116403.288	576975.169	1493.413	1467.467	0.013	0.035	1.2
Nal-19	37.19251586	-116.12774043	4116585.357	577414.934	1486.600	1460.655	0.014	0.042	1.0
Nal-20	37.19418066	-116.11980495	4116776.563	578117.525	1496.663	1470.720	0.017	0.021	1.0
Nal-21	37.22079420	-116.14084997	4119711.944	576222.962	1684.459	1658.610	0.014	0.034	1.2

Appendix B B.3

Pacific Northwest National Laboratory

902 Battelle Boulevard P.O. Box 999 Richland, WA 99354

1-888-375-PNNL (7665)

www.pnnl.gov